

1 **Supercooled Liquid Water Cloud observed, analysed and modelled**
2 **at the Top of the Planetary Boundary Layer above Dome C,**
3 **Antarctica**

4

5 **Philippe Ricaud¹, Massimo Del Guasta², Eric Bazile¹, Niramson Azouz¹, Angelo Lupi³,**
6 **Pierre Durand⁴, Jean-Luc Attié⁴, Dana Veron⁵, Vincent Guidard¹ and Paolo Grigioni⁶**

7

8 ¹CNRM, Université de Toulouse, Météo-France, CNRS, Toulouse, France

9 ²INO-CNR, Sesto Fiorentino, Italy

10 ³ISAC-CNR, Italy

11 ⁴Laboratoire d'Aérodynamique, Université de Toulouse, CNRS, UPS, Toulouse, France

12 ⁵University of Delaware, Newark, USA

13 ⁶ENEA, Roma, Italy

14

15

16

17 **Version V03.R2, 6 March 2020**

18

19 Submitted to ACPD

20

21

22 **Abstract**

23 A comprehensive analysis of the water budget over the Dome C (Concordia, Antarctica)
24 station has been performed during the austral summer 2018-2019 as part of the Year of Polar
25 Prediction (YOPP) international campaign. Thin (~100-m deep) supercooled liquid water
26 (SLW) clouds have been detected and analysed using remotely sensed observations at the
27 station (tropospheric depolarization LIDAR, microwave radiometer HAMSTRAD, net surface
28 radiation from Baseline Surface Radiation Network BSRN), radiosondes and using satellite
29 observations (CALIOP/CALIPSO) combined with a specific configuration of the Numerical
30 Weather Prediction model: ARPEGE-SH (Action de Recherche Petite Echelle Grande Echelle
31 – Southern Hemisphere). The analysis shows that SLW clouds were present from November to
32 March, with the greatest frequency occurring in December and January when ~50% of the days
33 in summer time exhibited SLW clouds for at least one hour. Two case studies are used to
34 illustrate this phenomenon. On 24 December 2018, the atmospheric planetary boundary layer
35 (PBL) evolved following a typical diurnal variation, which is to say with a warm and dry mixing
36 layer at local noon thicker than the cold and dry stable layer at local midnight. Our study showed
37 that the SLW clouds were observed at Dome C within the entrainment and the capping inversion
38 zones at the top of the PBL. ARPEGE-SH was not able to correctly estimate the ratio between
39 liquid and solid water inside the clouds with the Liquid Water Path (LWP) strongly
40 underestimated by a factor 1000 compared to observations. The lack of simulated SLW in the
41 model impacted the net surface radiation that was 20-30 W m⁻² higher in the BSRN observations
42 than in the ARPEGE-SH calculations, mainly attributable to the BSRN longwave downward
43 surface radiation being 50 W m⁻² greater than that of ARPEGE-SH. The second case study takes
44 place on 20 December 2018, when a warm and wet episode impacted the PBL with no clear
45 diurnal cycle of the PBL top. SLW cloud appearance within the entrainment and capping
46 inversion zones coincided with the warm and wet event. The amount of liquid water measured

47 by HAMSTRAD was ~ 20 times greater in this perturbed PBL than in the typical PBL. Since
48 ARPEGE-SH was not able to accurately reproduce these SLW clouds, the discrepancy between
49 the observed and calculated net surface radiation was even greater than in the typical PBL case,
50 reaching $+50 \text{ W m}^{-2}$, mainly attributable to the downwelling longwave surface radiation from
51 BSRN being 100 W m^{-2} greater than that of ARPEGE-SH. The model was then run with a new
52 partition function favouring liquid water for temperatures below -20°C down to -40°C . In this
53 test mode, ARPEGE-SH has been able to generate SLW clouds with modelled LWP and net
54 surface radiation consistent with observations during the typical case whereas, during the
55 perturbed case, the modelled LWP was 10 times less than the observations and the modelled
56 net surface radiation remained lower than the observations by $\sim 50 \text{ W m}^{-2}$. Accurately modelling
57 the presence of SLW clouds appears crucial to correctly simulate the surface energy budget
58 over the Antarctic Plateau.

59

60 **1. Introduction**

61 Antarctic clouds play an important role in the climate system by influencing the Earth's
62 radiation balance, both directly at high southern latitudes and, indirectly, at the global level
63 through complex teleconnections (Lubin et al., 1998). In Antarctica, there are very few
64 observational stations and most of them are located on the coast, a fact that limits the type and
65 characteristics of clouds observed. Nevertheless, prior studies suggest that cloud properties vary
66 geographically, with a fractional cloud cover around the South Pole of about 50 to 60% in all
67 seasons, and a cloud cover of about 80 to 90% near the coast (Bromwich et al., 2012; Listowski
68 et al., 2019). Based on spaceborne observations, Adhikari et al. (2012) observed that low-level
69 cloud occurrence over the Antarctic Plateau is consistently between 20-50% with the highest
70 values occurring in winter and the lowest values consistently occurring over the Eastern
71 Antarctic Plateau. Furthermore, cloud parameters such as the hydrometeors size and the
72 microphysical structure are also very difficult to retrieve in Antarctica. Nevertheless, some in
73 situ aircraft measurements exist particularly over the Western Antarctic Peninsula (Grosvenor
74 et al., 2012; Lachlan-Cope et al., 2016) and nearby coastal areas (O'Shea et al., 2017) that
75 provide ice mass fraction, concentration and particle size relative to cloud temperature, cloud
76 type and formation mechanism which have provided new insights to polar cloud modelling.
77 These studies also highlighted sea-ice production of Cloud-Condensation Nuclei and Ice
78 Nucleating Particles, which is important in winter both coastally and at Dome C (see e.g.
79 Legrand et al., 2016). Additionally, Grazioli et al. (2017) observed precipitating crystal
80 characteristics at Dumont d'Urville using a combination of ground-based radars, in situ cameras
81 and precipitation sensors, and looked at the role that the katabatic winds play in the formation,
82 modification and sublimation of ice crystals. Over the Antarctic Plateau, where the atmosphere
83 is colder and drier than along the coast, ice crystal clouds are mainly observed with crystal sizes
84 ranging from 5 to 30 μm (effective radius) in the core of the cloud; mixed-phase clouds are

85 preferably observed near the coast (Listowski et al., 2019) with larger ice crystals and water
86 droplets (Lachlan-Cope, 2010; Lachlan-Cope et al., 2016; Grosvenor et al., 2012; O’Shea et al.,
87 2017; Grazioli et al., 2017).

88 The time and geographical distribution of tropospheric clouds over the Antarctic region
89 has been recently studied using the raDAR/liDAR-MASK (DARDAR) spaceborne products
90 (Listowski et al., 2019). The authors determined that clouds are mainly constituted of ice above
91 the continent. The presence of Supercooled Liquid Water (SLW, the water staying in liquid
92 phase below 0°C) clouds shows variations according to temperature and sea ice fraction,
93 decreasing sharply poleward, with an abundance two to three times less over the Eastern
94 Antarctic Plateau than over the Western Antarctic. The inability of mesoscale high-resolution
95 models and operational numerical weather prediction models to accurately calculate the net
96 surface radiation due to the presence of clouds (particularly of SLW clouds) in Antarctica
97 causes biases of several tens of watt per square meters (Listowski and Lachlan-Cope, 2017,
98 King et al., 2006, 2015; Bromwich et al., 2013) impacting the radiative budget of the Antarctic
99 and beyond (Lawson and Gettelman, 2014; Young et al. 2019). The year-long study of mixed-
100 phase clouds at South Pole with a micropulse LIDAR presented in Lawson and Gettelman
101 (2014) showed that SLW clouds occur more frequently than observed in earlier aircraft studies,
102 and are underestimated in models leading to biases in the surface radiation budget. In the present
103 study, we explore these biases further, moving the focus to the modelling and simultaneous
104 observations of low-level SLW clouds and surface radiation over the Eastern Antarctic Plateau,
105 specifically at Dome C.

106 With the support of the World Meteorological Organization (WMO) World Weather
107 Research Programme (WWRP), the Polar Prediction Project (PPP) international programme
108 has been dedicated to the development of improved weather and environmental prediction
109 services for the polar regions, on time scales from hours to seasons

110 (<https://www.polarprediction.net>). Within this project, the Year of Polar Prediction (YOPP),
111 from 2018 to 2019, aims at enabling a significant improvement in environmental prediction
112 capabilities for the polar regions and beyond, by coordinating a period of intensive observing,
113 modelling, verification, user-engagement and educational activities. The Water Budget over
114 Dome C (H₂O-DC) project (<https://apps3.awi.de/YPP/pdf/stream/52>) has been endorsed by
115 YOPP for studying the water budget by means of ground-based measurements of water (vapour,
116 solid and liquid) and clouds, by active (backscatter LIDAR) and passive (microwave
117 radiometer) remote sensing, and operational meteorological analyses. The Dome C (Concordia)
118 station is located in the Eastern Antarctic Plateau (75°06'S, 123°21'E, 3233 m above mean sea
119 level, amsl).

120 H₂O-DC concentrates on the Year of Polar Prediction Special Observing Period of
121 measurements in the Antarctic (SOP-SH), from 16 November 2018 to 15 February 2019.
122 During this time frame, several instruments have been employed.

123 1) The H₂O Antarctica Microwave Stratospheric and Tropospheric Radiometer
124 (HAMSTRAD, Ricaud et al., 2010a) to obtain vertical profiles of temperature and water
125 vapour, Integrated Water Content (IWC) or precipitable water, and Liquid Water Path (LWP),
126 with an adjustable time resolution fixed at 60 seconds during the YOPP campaign.

127 2) The tropospheric depolarization LIDAR (Tomasi et al., 2015) to obtain vertical profiles
128 of backscattering and depolarization ratio.

129 These two H₂O-DC data sets have been complemented in the present analysis by the 3
130 following observational datasets.

131 3) The Baseline Surface Radiation Network (BSRN) net surface radiances at the station.

132 4) The temperature profiles from radiosondes launched twice daily at the station during
133 YOPP.

134 5) The spaceborne observations (backscatter and polarization) from the
135 CALIOP/CALIPSO LIDAR in the vicinity of the station.

136 In addition, a specific Antarctic configuration of the global ARPEGE model from Météo-
137 France (Pailleux et al., 2015) is used to characterize the water budget above Dome C
138 considering the gas, liquid and solid phases to study the genesis of clouds (ice/liquid).

139 The aim of the present study is to combine all these observations and simulations in order
140 to 1) detect the presence of SLW clouds above Dome C, 2) analyse the formation and evolution
141 of such SLW clouds and 3) estimate the radiative impact of such clouds on the net surface
142 radiation. We concentrate the analyses on two case studies observed during the YOPP
143 campaign: one case when the Planetary Boundary Layer (PBL) exhibited a “typical” diurnal
144 cycle (24 December 2018) and a second case when the diurnal cycle of the PBL was perturbed
145 by a warm and wet episode (20 December 2018).

146 The data sets used in our study are presented in section 2. The methodology employed is
147 explained in section 3. The analyses of the SLW clouds during the typical and the perturbed
148 PBL periods are detailed in sections 4 and 5, respectively. The observed and modelled impact
149 of SLW clouds on the surface net radiation is described in section 6. Section 7 includes a
150 discussion of the results and the conclusion synthesizes the study in section 8.

151

152 **2. Datasets**

153 **2.1. The HAMSTRAD Radiometer**

154 HAMSTRAD is a microwave radiometer that profiles water vapour (H₂O), liquid water and
155 tropospheric temperature above Dome C. Measuring at both 60 GHz (oxygen molecule line
156 (O₂) to deduce the temperature) and 183 GHz (H₂O line), this unique, state-of-the-art
157 radiometer was installed on site for the first time in January 2009 (Ricaud et al., 2010a and b).
158 The measurements of the HAMSTRAD radiometer allow the retrieval of the vertical profiles

159 of H₂O and temperature from the ground to 10-km altitude with vertical resolutions of 30 to 50
160 m in the PBL, 100 m in the free troposphere and 500 m in the upper troposphere-lower
161 stratosphere. The time resolution is adjustable and fixed at 60 seconds during the YOPP
162 campaign. Note that an automated internal calibration is performed every 12 atmospheric
163 observations and lasts about 4 minutes. Consequently, the atmospheric time sampling is 60
164 seconds for a sequence of 12 atmospheric measurements and a new atmospheric sequence is
165 performed after 4 minutes. The temporal resolution on the instrument allows for detection and
166 analysis of atmospheric processes such as the diurnal evolution of the PBL (Ricaud et al., 2012)
167 and the presence of clouds and diamond dust (Ricaud et al., 2017). In addition, two other
168 parameters can be estimated.

169 1) The Integrated Water Vapour (IWV) or precipitable water (kg m^{-2}) obtained by
170 integrating the absolute humidity profile from the surface to 10 km altitude.

171 2) The Liquid Water Path (g m^{-2}) that gives the amount of liquid water integrated along the
172 vertical.

173 IWV has been validated against radiosondes at Dome C between 2010 and 2014 showing a
174 5-10% wet bias of HAMSTRAD compared to the sondes (Ricaud et al., 2015) that were
175 uncorrected for sensor heating or time lag effect that may produce a 4% dry bias (Miloshevich
176 et al., 2006). The 1- σ RMS error on the 7-min integration time IWV is 0.05 kg m^{-2} or $\sim 5\%$
177 (Ricaud et al., 2013).

178 The HAMSTRAD-observed LWP has only been presented when the instrument was
179 installed at the Pic du Midi station (2877 amsl, France) during the calibration/validation period
180 in 2008 prior to its set up in Antarctica in 2009 (Ricaud et al., 2010a). Because the instrument
181 has been designed and developed for measuring water vapour in very dry and cold environments
182 such as those encountered at the Dome C station all year long, the radiometer functionality is
183 better adapted for the Dome C site than for the Pic du Midi site. It has not been possible to

184 validate LWP observations at the Pic du Midi station. The H₂O-DC project has thus provided a
185 unique opportunity to perform such a qualitative validation against LIDAR observations of
186 SLW.

187

188 **2.2. The tropospheric depolarization LIDAR**

189 A tropospheric depolarization LIDAR (532 nm) has been operating at Dome C since 2008
190 (see http://lidarmax.altervista.org/englidar/_Antarctic%20LIDAR.php). The LIDAR provides
191 5-min tropospheric profiles of aerosols and clouds continuously, from 20 to 7000 m above
192 ground level (agl), with a resolution of 7.5 m. LIDAR depolarization (Mishchenko et al., 2000)
193 is a robust indicator of non-spherical shape for randomly oriented cloud particles. A
194 depolarization ratio below 10% is characteristic of SLW clouds, while higher values are
195 produced by ice particles. The possible ambiguity between SLW clouds and oriented ice plates
196 is avoided at Dome C by operating the LIDAR 4° off-zenith (Hogan and Illingworth, 2003).
197 The LIDAR observations at Dome C have already been used to study the radiative properties
198 of water vapour and clouds in the far infrared (Palchetti et al., 2015). As a support to LIDAR
199 data interpretation, time-lapse webcam videos of local sky conditions are also collected.

200

201 **2.3. The BSRN Network**

202 The BSRN sensors at Dome C are mounted at the Astroconcordia/Albedo-Rack sites, with
203 upward and downward looking, heated and ventilated standard Kipp&Zonen CM22
204 pyranometers and CG4 pyrgeometers providing measurements of hemispheric downward and
205 upward broadband shortwave (SW, 0.3–3 μm) and longwave (LW, 4–50 μm) fluxes at the
206 surface, respectively. These data are used to retrieve values of net surface radiation (defined as
207 the difference between the downward and upward fluxes). All these measurements follow the
208 rules of acquisition, quality check and quality control of the BSRN (Driemel et al., 2018).

209

210 **2.4. Radiosondes**

211 Vertical temperature and humidity profiles have been measured on a daily basis at Dome C
212 since 2005, employing RS92 Vaisala radiosondes. The radiosonde data were taken using the
213 standard Vaisala evaluation routines without any correction of sensor heating or time lag effect.
214 The sondes are known to have a cold bias of 1.2 K from the ground to about 4 km altitude
215 (Tomasi et al., 2011 and 2012) and a dry bias of 4% on IWV (Miloshevish et al., 2006), mainly
216 between 630 and 470 hPa, with a correction factor for humidity varying within 1.10–1.15 for
217 daytime (Miloshevish et al., 2009). During YOPP and the two case studies, launches were
218 performed twice per day at 00:00 and 12:00 UTC.

219

220 **2.5. CALIOP on board CALIPSO**

221 Orbiting at 705-km altitude, the CALIPSO (Cloud Aerosol Lidar and Infrared Pathfinder
222 Satellite Observations) mini-satellite has been observing clouds and aerosols since 2006 to
223 better understand the role of clouds and aerosols in climate. To accomplish this mission, the
224 CALIPSO satellite is equipped with a LIDAR, a camera and an infrared imager (Winker et al.,
225 2009). CALIOP (Cloud-Aerosol Lidar with Orthogonal Polarization) is a dual-wavelength (532
226 and 1064 nm) backscatter LIDAR. It provides high-resolution vertical profiles of clouds and
227 aerosols along the orbit track (Young et al., 2009). We have used version V3.40 data retrieved
228 from <https://www-calipso.larc.nasa.gov/>.

229

230 **2.6. The ARPEGE-SH Model**

231 A special Antarctic configuration of the operational global model ARPEGE was used for
232 the YOPP SOP-SH period (16/11/2018–15/02/2019). This configuration named ARPEGE-SH
233 is based on the operational global model used for Numerical Weather Prediction (NWP)

234 ARPEGE (Pailleux et al., 2015), but with its highest horizontal resolution centred over Dome
235 C instead of over France, as set up in ARPEGE. A 4D variational (4DVar) assimilation was
236 performed every 6 h. The meteorological analyses were given by the ARPEGE-SH system
237 together with the 24-hour forecasts at the node the closest to the location of Dome C. Two
238 analyses at 00:00 and 12:00 UTC were represented in the present study together with hourly
239 forecasts initialized by the two analyses from 01:00 to 11:00 and from 13:00 to 24:00 UTC,
240 respectively. The horizontal resolution during the SOP-SH period was 7.5 km at Dome C. The
241 vertical resolution during the SOP-SH period was constituted by 105 vertical levels, the first
242 one being set at 10 m, with 12 levels below 1 km and 35 levels below 3 km. Several ARPEGE-
243 SH output parameters were selected for analysis: cloud fraction, ice, water vapour and liquid-
244 water mixing ratio, temperature, Total Column Ice (TCI, ice integrated along the vertical),
245 LWP, IWV, and net surface radiation. For each of the model vertical level, the value of the
246 cloud fraction ranges between 0 and 1 and is defined as the fraction of the cloud within the
247 model horizontal grid box. The total cloud fraction at each level is a combination between the
248 resolved cloud, the cloud from the shallow convection and the cloud from the deep convection.
249 The resolved cloud is based on a pdf function with critical relative humidity profile. The shallow
250 convection cloud (below 4000 m) is based on the cloud water/ice tendencies computed by the
251 shallow mass flux scheme with a maximum value at 0.3. For the deep convection, the cloudiness
252 is computed with the vertical divergence of the precipitation flux. The diurnal variation of the
253 top of the PBL is calculated by ARPEGE-SH as the level where the turbulence kinetic energy
254 becomes lower than $0.01 \text{ m}^2 \text{ s}^{-2}$.

255

256 **2.7. The NCEP temperature fields**

257 In order to assess the synoptic state of the atmosphere during the two case studies above
258 Dome C against the climatological state of the atmosphere in summer over Antarctica, we have

259 used the temperature fields at 600 hPa from the National Centers for Environmental Prediction
260 (NCEP) from 2009 to 2019 (Kanamitsu et al., 2002). These are NCEP-Department of Energy
261 (NCEP/DOE) Atmospheric Model Intercomparison Project (AMIP-II) Reanalysis (Reanalysis-
262 2) 6-hourly air temperature at 2.5°x2.5° horizontal resolution over the globe.

263

264 **2.8. The HYSPLIT back-trajectories**

265 In order to assess the origin of airmasses associated to the two case studies, ten-day back-
266 trajectories originated from the Dome C station at 500 and 1000 m above ground level have
267 been calculated on 20 and 24 December 2018 at 12:00 UTC from the Hybrid Single-Particle
268 Lagrangian Integrated Trajectory model (HYSPLIT) model (Stein et al., 2015; Rolph et al.,
269 2017) (<https://www.ready.noaa.gov/HYSPLIT.php>).

270

271 **3. Methodology**

272 In this article, we present two case studies from the SOP-SH that illustrate the occurrence
273 of low-level SLW clouds at Dome C. Both cases occurred in December 2018, within 5 days of
274 each other, which allows direct comparison between the cases without concerns for seasonal
275 variations in radiation.

276 The first case study presented was on 24 December 2018 and was representative of a
277 climatological summer atmosphere in contrast to the second case study (20 December 2018)
278 when the atmosphere was very different from a climatological summer atmosphere. We have
279 considered in Figure 1 the temperature fields from the NCEP at 600 hPa to highlight the state
280 of the atmosphere above Antarctica with a focus over the Dome C station at different periods:
281 a) decadal average over December-January from 2009 to 2019, b) YOPP average over
282 December 2018-January 2019, c) daily average over 24 December 2018, d) 20 December 2018
283 at 00:00 UTC, e) 20 December 2018 at 12:00 UTC, and f) 21 December 2018 at 00:00 UTC.

284 The climatological summer temperature field at 600 hPa has been calculated by averaging the
285 December and January data from 2009 to 2019 and the mean synoptic state of the YOPP
286 campaign during the summer 2018-2019 has been calculated by averaging data from early
287 December 2018 to end of January 2019. The synoptic state of the first case study was selected
288 on 24 December 2018 averaged from 00:00 to 24:00 UTC and for the second case study on 20
289 December 2018 at 00:00 UTC and 12:00 UTC, and on 21 December 2018 at 00:00 UTC. Firstly,
290 the summer atmosphere during YOPP was very consistent with the decadal climatological state
291 of the atmosphere both over Antarctica and the Dome C station (temperature less than 245 K).
292 Secondly, the synoptic state of the atmosphere on 24 December 2018 (1st case study), although
293 warmer (> 258 K) over some parts of the Antarctic Plateau (60°E - 90°E) is, over Dome C,
294 consistent with the YOPP summer synoptic state and the climatological summer temperatures
295 of ~ 246 K. Thirdly, on 20 December 2018 (2nd case study), on tongue of warm air (254-260 K)
296 originated from the oceanic coast in the sector 0 - 30°W (00:00 UTC) reaches Dome C 24 hours
297 later with temperatures increasing from 252 to 256 K, about 10 K greater than on 24 December
298 2018. Ten-day back trajectories calculated from HYSPLIT (see Figure Supp1) initiated at
299 Dome at 500 and 1000 m above ground level remain over the Antarctic Plateau on 24 December
300 2018 (1st case study) whereas are originated to the oceanic coast in the sector 0 - 30°W on 20
301 December 2018 (2nd case study). This is consistent with previous studies (Ricaud et al., 2017)
302 showing that inland-originated air masses bring cold and dry air to Dome C whilst ocean-
303 originated air masses bring warm and wet air to Dome C.

304 In the following, we will label the 1st case study on 24 December 2018 as typical case and
305 the 2nd case study as perturbed case. We will show that, in the typical case, the SLW cloud
306 occurred over a 24-hour period that was characterized by a typical summertime, diurnal PBL
307 cycle, where the mixed-layer develops over the course of the day, reaches a quite stable height
308 and then collapses to the surface toward the end of the day, around 12 UTC (Ricaud et al.,

309 2012). The first case provides insight into the impact of SLW clouds on the local radiative
310 fluxes. The perturbed case provides a contrasting situation where the diurnal cycle of the PBL
311 was perturbed by the sudden arrival of very moist and warm air of oceanic origin (see Ricaud
312 et al., 2017). We analyse how this episode affected the presence and evolution of SLW clouds
313 and their influence on the surface energy budget. Note that, in the remaining of the article, the
314 data will be presented according to their height above ground level (agl) unless explicitly shown
315 as above mean sea level (amsl).

316

317 **4. Typical diurnal cycle of the PBL**

318 The first case study occurred on 24 December 2018 during a typical diurnal PBL cycle.
319 All the results are presented in Universal Time Coordinated (UTC) with local time (LT) being
320 eight hours ahead of UTC ($LT = UTC + 8 \text{ hr}$). As described in Ricaud et al. (2012), the typical
321 summer boundary layer at Dome C is very similar to that described by Stull (1988). Although
322 sunlight is present throughout the day, the variation in magnitude is enough to allow a stable
323 boundary layer from 18:00 to 06:00 LT, similar to a stable nocturnal boundary layer. There is
324 then a transition from a stable boundary layer to a mixed layer around 06:00 LT with the
325 increase in the solar irradiation, which reaches a maximum around solar noon. Then around
326 18:00 LT, the stable boundary layer starts to form again, with a quasi-mixed layer about it. The
327 height of the summertime boundary layer at Dome C typically ranges between 100 and 400 m.
328 The presence of SLW clouds at the top of the PBL together with the diurnal evolution of the
329 PBL will be discussed in more detail in the section 7.2.

330

331 **4.1. Clouds**

332 The presence of clouds is highlighted by the LIDAR backscatter and depolarization profiles
333 shown in Figures 2a and b, respectively. High values of LIDAR backscatter ($\beta > 100 \beta_{\text{mol}}$, with

334 β_{mol} the molecular backscatter) indicate that clouds and/or precipitation are present
335 intermittently throughout the day with some significant differences. First, vertical “stripes” of high
336 backscatter values are visible from 10 to 400 m height before 10:00 UTC and after 19:00 UTC,
337 associated with high values of depolarization ratio ($> 20\%$), characteristic of precipitating ice
338 crystals. Second, high values of β associated with very low depolarization ratio ($< 5\%$) occur
339 within a thin layer of approximately 100-m depth around 500 m from 08:00 to 22:00 UTC, with
340 some breaks around 11:00 and 19:00-21:00 UTC. From the LIDAR observations, this
341 combination of high backscatter and low depolarization ratio signifies the presence of a SLW
342 cloud (Figure 2c).

343 The NWP model ARPEGE-SH calculates cloud fraction, ice water and liquid water mixing
344 ratios (kg kg^{-1}) for 24 December 2018 (Figures 3a, b and c, respectively). We note that the
345 outputs from ARPEGE-SH at 00:00 and 12:00 UTC are the analyses and, for the remaining
346 time, the outputs are the hourly forecasts. ARPEGE-SH predicts the presence of clouds (cloud
347 fraction > 0.95) for most of the day except around 11:00 and 23:00 UTC (Fig. 3a). Before 12:00
348 UTC, the cloud is mainly confined between 300 and 600-800 m whilst, after 12:00 UTC, it
349 spreads from the surface to 800 m. There are also high-level clouds at 2000-3000 m height but
350 with a cloud fraction between 0.50 and 0.70. The majority of the clouds produced by ARPEGE-
351 SH are mainly composed of ice crystals (Fig. 3b) with some traces of droplets (Fig. 3c) due to
352 the model’s partitioning between ice and liquid where all condensed water is ice below -20°C .
353 The liquid water clouds derived from the LIDAR observations are superposed over the SLW
354 clouds calculated by ARPEGE-SH. The modelled values of liquid water ($\sim 4 \cdot 10^{-6} \text{ g m}^{-3}$) are very
355 low, far lower than the values of 0.1 g m^{-3} observed for coastal polar stratus clouds (see e.g.
356 O’Shea et al., 2017; Lachlan-Cope et al., 2016; Young et al., 2016). It is evident that ARPEGE-
357 SH fails in estimating: 1) the vertical distribution of liquid water (a thin layer is observed around
358 500 m whereas the modelled cloud layer extends from the surface to 800 m); 2) its temporal

359 evolution (presence of SLW cloud almost all day long in ARPEGE-SH compared to SLW
360 clouds from 08:00 to 22:00 UTC in the observations); and 3) the liquid vs. ice mixing ratio, the
361 former being in the model several orders of magnitudes lower than the latter, in contrast to the
362 observations.

363 The diurnal variation along the vertical of the Total Snow Flux (mm day^{-1}) calculated by
364 ARPEGE-SH on 24 December 2018 and on 20 December 2018 is shown on Figures Supp2 and
365 Supp3, respectively. On 24 December 2018 (Fig. Supp2), ARPEGE-SH forecasts some solid
366 precipitation between 00:00 and 10:00 UTC from ~ 500 m agl to the surface consistently with
367 the LIDAR observations (Figs. 2a and b). On 20 December 2018 (Fig. Supp3), ARPEGE-SH
368 calculates trace amounts of solid precipitation close to the surface around 16:00 UTC
369 consistently with the LIDAR observations (Figs. 9a and b). ARPEGE-SH was thus able to
370 forecast solid precipitation during the 2 case studies.

371 The presence of clouds above the station can also be inferred from vertically-integrated
372 variables such as: 1) TCI calculated by ARPEGE-SH, 2) LWP from HAMSTRAD and
373 ARPEGE-SH, and 3) IWV from HAMSTRAD and ARPEGE-SH (Figures 4a, b and c,
374 respectively). The ARPEGE-SH TCI on 24 December 2018 (Fig. 4a) oscillates between 10 and
375 30 g m^{-2} except around 12:00 UTC when a clear minimum occurs ($\sim 3 \text{ g m}^{-2}$), underscoring the
376 fact that ARPEGE-SH obtains ice clouds for the entire day, except at 12:00 UTC. The
377 HAMSTRAD LWP shows an obvious increase from ~ 1.0 to $\sim 2.0\text{-}3.0 \text{ g m}^{-2}$ when the presence
378 of SLW cloud is indicated by LIDAR observations (Fig. 4b). The ARPEGE-SH LWP is, on
379 average, 10^3 times lower than that observed by HAMSTRAD, highlighting the fact that
380 ARPEGE-SH misrepresents features of the SLW clouds over Dome C. The $1\text{-}\sigma$ RMS error on
381 the 1-min integration time for the HAMSTRAD LWP can be estimated to be $\sim 15\%$. Based on
382 the comparisons between the HAMSTRAD LWP and the LIDAR observations of SLW clouds
383 during the YOPP campaign, we can estimate that the LWP bias is about 1.0 g m^{-2} . We cannot

384 rule out that these biases might also be related in part to differences in the observation
385 wavelengths employed (submicrons for the LIDAR and microwaves for HAMSTRAD) that
386 could favour large particles (HAMSTRAD) against small particles (LIDAR). Biases might also
387 be due to the observing geometry that differs between the LIDAR (close to zenith viewing) and
388 HAMSTRAD (atmospheric scans at 10 angles from zenith to $\sim 3^\circ$ elevation). HAMSTRAD and
389 ARPEGE-SH IWV (Fig. 4c) vary from 0.65-1.05 kg m⁻² throughout the day on 24 December
390 2018, with an agreement to within 0.1 kg m⁻² (i.e. ~ 10 -15%), which is consistent with previous
391 studies (Ricaud et al., 2017).

392 Observation of clouds from space-borne sensors has two main advantages: 1) it
393 complements the ground-based cloud observations at Dome C (namely ice/liquid water), and
394 2) it provides an estimate of the vertical and horizontal extents of the detected cloudy layers.
395 Note that the CALIPSO spaceborne LIDAR operates at the same wavelength as the backscatter
396 LIDAR at Dome C, with the same method for discriminating ice from liquid water.
397 Consequently, the two LIDARs should give consistent information for the detected cloud phase.
398 However, the presence of an optically thick cloud may extinguish the CALIOP signal
399 underneath as was already presented in Ricaud et al. (2017) when studying episodes of thick
400 (5-km deep) clouds and diamond dust (ice crystals in suspension close to the surface). The main
401 difficulty with this approach is related to the temporal and spatial sampling of the spaceborne
402 instrument, namely finding a satellite overpass coincident both in time and location with the
403 cloud observed at Dome C. This, unfortunately, decreases the number of overpasses that is
404 scientifically exploitable. Nevertheless, on 24 December 2018, 2 orbits of CALIOP/CALIPSO
405 passed close to Dome C at times when SLW clouds were observed by ground-based
406 instruments. We show the vertical feature mask and ice/water phase from the pass closest to the
407 station (~ 220 km), from 15:50 to 16:03 UTC (Figures 5a and b, respectively). Firstly, we note
408 the presence of a cloud a few hundred meters deep near the surface in the vicinity of Dome C

409 (Fig. 5a; note that the CALIOP/CALIPSO altitude is above sea level and Dome C is at an
410 altitude of 3233 m amsl). Secondly, this cloud is composed of SLW (Fig. 5b), confirming the
411 analysis based on the observations from the LIDAR and the HAMSTRAD radiometer.
412 Furthermore, we can state that this SLW cloud is not a local phenomenon but has a horizontal
413 extent of ~450 km along the orbit track. Considering the CALIOP total and perpendicular
414 attenuated backscatter data at 532 nm on 24 December 2018 at 16:00 and 14:00 UTC (Figures
415 Supp4 and Supp5, respectively), we note that: 1) the SLW cloud is located between 3.7 and 3.8
416 km amsl, that is to say a height from ~450 to ~550 m agl, and 2) since the CALIOP signal is
417 able to reach the surface underneath the SLW cloud, ice is not detected by the space-borne
418 instrument. This is consistent with the observations performed at Dome C. The other orbit from
419 14:11 to 14:25 UTC (Figure Supp6) is slightly more distant than the one shown in Figure 5
420 (~360 km), but it exhibits a similar SLW cloud located between ~450 and ~550 m agl, over an
421 even greater horizontal extent of ~700 km along the orbit track.

422

423 **4.2. Vertical profiles of temperature and water vapour**

424 On 24 December 2018, temperatures from both HAMSTRAD and ARPEGE-SH ranged
425 from 240 to 250 K (-33 to -23°C) from the surface to 1-km agl, compatible with the presence
426 of SLW clouds. The diurnal variations of temperature and water vapour anomalies calculated
427 by ARPEGE-SH and measured by HAMSTRAD are shown in Figure 6. For each height, the
428 daily-averaged value has been subtracted. This has the advantages of highlighting areas of
429 maximum and minimum changes along the vertical, and reduces biases when comparing the
430 two data sets. Absolute anomalies (K) are presented for temperatures whilst relative anomalies
431 (%) are shown for water vapour.

432 The diurnal variation of the ARPEGE-SH temperature (Fig. 6a) from the surface to 1 km
433 shows a warm atmosphere before 12:00 UTC and a fast cooling one afterward. HAMSTRAD

434 shows a similar cooling (Fig. 6b), but the transition is not so abrupt and occurs later, around
435 15:00 UTC. The diurnal amplitude is greater in ARPEGE-SH (~5 K) than in HAMSTRAD (~3
436 K). The diurnal variation of the water vapour in ARPEGE-SH (Fig. 6c) from the surface to 1
437 km shows a wet atmosphere before 12:00 UTC and a drier atmosphere after, again with an
438 abrupt transition. From HAMSTRAD, the diurnal variation of the water vapour (Fig. 6d) from
439 the surface to 1 km is more complex, alternating wet and dry phases, which is particularly
440 obvious at 500-m altitude: wet (00:00-03:00 UTC), dry (03:00-08:00 UTC), wet (08:00-09:00
441 UTC), dry (09:00-12:00 UTC), wet (12:00-22:00 UTC) and dry (22:00-24:00 UTC). The time
442 evolution of the SLW cloud (Fig. 2c) and the diurnal variation of the top of the PBL as
443 calculated by ARPEGE-SH are superposed on all the panels of Figure 6. We note that the SLW
444 cloud appeared just below the ARPEGE-SH-estimated PBL top, around 08:00 UTC, and
445 persisted around the same altitude after 12:00 UTC even though the PBL top had dramatically
446 decreased down to the surface. In addition, the SLW cloud persisted after 12:00 UTC in a layer
447 that is cooler than earlier in the day, but slightly warmer than the air above and below it.
448 However, the model shows that this layer is drier while the observations suggest it is wetter.

449

450 **4.3. Potential Temperature Gradient**

451 We now consider the mechanisms that allow the SLW cloud to persist in a thin layer (about
452 100-m deep) around 500-600 m altitude. Even if the PBL gets thinner after 12:00 UTC, a
453 residual mixed layer remains above (see e.g. Figure 1.7 of Stull, 2012; Figure 12 top of Ricaud
454 et al., 2012 and definition of a residual layer from the American Meteorological Society at
455 http://glossary.ametsoc.org/wiki/Residual_layer). This layer, where turbulence is sporadic or
456 even absent, lies above the surface-connected stable layer, and can be viewed as a fossil of the
457 mixed layer developed during the previous mixing period. The transition from the boundary

458 layer to the free atmosphere is characterized by a local maximum of the potential temperature
459 (θ) vertical gradient ($\partial\theta/\partial z$).

460 Figure 7 shows $\partial\theta/\partial z$ field and the evolution of the mixed layer top, both computed from
461 ARPEGE-SH output – the latter defined according to whether the turbulent kinetic energy
462 exceeds a defined threshold – and the observed SLW cloud superposed. Black areas correspond
463 to neutral conditions ($\partial\theta/\partial z \sim 0$), whereas the coloured ones relate to stable stratification
464 according to the colour scale in the Figure. The SLW cloud, once appeared at the top of the
465 PBL around 08:00 UTC, persists after 12:00 UTC in a layer around 500-600 m coinciding with
466 the top of the residual mixed layer (see above for the definition) even after the ARPEGE-defined
467 mixed layer top collapses down to the surface.

468 Figures 8a, b and c show the vertical profiles of θ (K) and $\partial\theta/\partial z$ (K km⁻¹) as calculated
469 from temperature measured by the radiosondes and analysed by ARPEGE-SH at Dome C on
470 24 December 2018 at 00:00 and 12:00 UTC and on 25 December 2018 at 00:00 UTC,
471 respectively. The presence and the depth of the SLW cloud detected from LIDAR observations
472 are highlighted in the Figure. The atmosphere as analysed by ARPEGE-SH is about 3-5 K
473 warmer than the observations. From 100 m upward, the maximum of $\partial\theta/\partial z$ is measured at 400,
474 550 and 600 m on 24 December 2018 at 00:00 and 12:00 UTC and on 25 December 2018 at
475 00:00 UTC, respectively with an amplitude of 10, 12 and 40 K km⁻¹, respectively. ARPEGE-
476 SH cannot reproduce the fine vertical structure of $\partial\theta/\partial z$. For example, the simulated maxima
477 of $\partial\theta/\partial z$ (Fig. 8) are slightly higher (600, 700 and 600 m for the same dates, respectively) and
478 less intense than those of radiosondes (8, 8 and 18 K km⁻¹, respectively).

479

480 **5. Perturbed diurnal cycle of the PBL**

481 On the second case study, 20 December 2018, the diurnal cycle of the PBL was perturbed
482 by the sudden arrival of very moist, warm air of oceanic origin. During this warming period,

483 the boundary layer remains mixed and does not form a stable boundary layer even when the
484 solar forcing decreases. This will be discussed in detail in the section 7.2.

485

486 **5.1. Clouds**

487 As in section 3.1, the high LIDAR backscatter ($\beta > 100 \beta_{\text{mol}}$) and low depolarization
488 (<5%) showed the presence of SLW clouds (Figures 9a, b and c, respectively). Before 13:00
489 UTC, there is no trace of clouds above Dome C, while from 13:00 to 23:00 UTC SLW clouds
490 are detected between 200 and 600 m. On all panels, we superimposed the PBL top calculated
491 by the ARPEGE-SH model. We note that the PBL top does not drop to the surface after 12:00
492 UTC as typically occurs, like on 24 December 2018, but rather remains between 100 and 200
493 m. Consistent with the conclusions derived from the observations of 24 December 2018, the
494 SLW cloud, once present, stays just above the height of the PBL top.

495 The cloud fraction, ice water and liquid water mixing ratios (kg kg^{-1}) calculated by
496 ARPEGE-SH on 20 December 2018 are shown in Figures 10a, b and c, respectively. Contrary
497 to the observations, the model simulates mixed-phase clouds (maximum cloud fraction of
498 ~30%), mainly composed of ice, prior to 12:00 UTC; from 00:00 to 06:00 UTC, the clouds are
499 forecasted below the PBL top. After 12:00 UTC, clouds appear 1-2 hours later in the model
500 than in the observations, at 14:00-15:00 UTC, just below the PBL top (maximum cloud fraction
501 of ~100%). The modelled cloud is mainly composed of ice with some traces of SLW above the
502 PBL around 15:00-16:00 UTC. In all occurrences, the liquid water amounts produced by the
503 model are extremely small, nearly non-existent. We note the presence of high altitude cirrus
504 (ice) clouds calculated by ARPEGE-SH after 12:00 UTC around 3-4 km height, while not
505 observed likely because the LIDAR light is attenuated by the SLW layer. As on 24 December
506 2018, the model fails to reproduce the presence of the SLW layer observed by the LIDAR near
507 the PBL top.

508 The diurnal evolutions of the TCI calculated by ARPEGE-SH, the LWP from
509 HAMSTRAD and ARPEGE-SH, and the IWV from HAMSTRAD and ARPEGE-SH on 20
510 December 2018 are presented in Figures 11a, b and c, respectively, with the presence of SLW
511 clouds derived from the LIDAR observations superimposed on Fig. 11b. Ice clouds are
512 calculated by ARPEGE-SH mainly around 15:00-16:00 UTC, with TCI values comparable to
513 those on 24 December 2018. SLW clouds are deduced from HAMSTRAD LWP between 13:00
514 and 23:00 UTC which coincides well with the SLW clouds observed by the LIDAR. The
515 maximum LWP values observed during this episode are much higher ($\sim 50 \text{ g m}^{-2}$) than on 24
516 December 2018 ($\sim 2\text{-}3 \text{ g m}^{-2}$). Again, the ARPEGE-SH LWP is negligible ($\sim 10^3$ times less than
517 observations). In parallel with the rapid increase of LWP, the observed IWV also jumps from
518 ~ 0.5 to $\sim 2.3 \text{ kg m}^{-2}$ within one hour after 13:00 UTC. ARPEGE-SH also calculates an increase
519 of IWV but lagged by one hour and much less intense ($\sim 1.3 \text{ kg m}^{-2}$). Additionally, the model
520 produces a systematically dryer atmosphere compared to HAMSTRAD by about 0.5 kg m^{-2}
521 after 16:00 UTC, although before the cloudy period that starts at 12:00 UTC, ARPEGE-SH and
522 HAMSTRAD IWV are consistent to within $\pm 0.2 \text{ kg m}^{-2}$.

523 On 20 December 2018, after 13:00 UTC when SLW clouds have been detected at Dome
524 C, both CALIPSO overpasses are far away from Dome C and, for the closest overpass at 13:17
525 UTC (closest distance to Dome C is 500 km), a very thick ice cloud at about 3 km agl prevents
526 the LIDAR radiation from reaching the surface (Figure Supp7). Unfortunately, no meaningful
527 information can be ascertained from the spaceborne observations on that day relevant to SLW
528 clouds in the vicinity of Dome C.

529

530 **5.2. Vertical profiles of temperature and water vapour**

531 The diurnal variations of the temperature and water vapour anomalies on 20 December
532 2018 as calculated by ARPEGE-SH and measured by HAMSTRAD are shown in Figure 12. In

533 ARPEGE-SH, a sharp transition between a warm and a cool atmosphere is evident at 12:00
534 UTC below the top of the PBL. In HAMSTRAD, from 00:00 to 06:00 UTC, the atmosphere
535 starts warming and then from 06:00 to 13:00 UTC, cools gradually to a minimum. After 13:00
536 UTC, HAMSTRAD temperatures reveal a warming starting from the surface and progressively
537 thickening until reaching the top of the PBL by the end of the day. Above the PBL, the
538 HAMSTRAD-observed and ARPEGE-SH-calculated temporal evolution of temperature and
539 water vapour are in an overall agreement. In the PBL, the model simulates a moistening around
540 05:00 UTC, but the most striking event is a sudden drying at 12:00 UTC. In HAMSTRAD,
541 there is a continuous drying from 00:00 UTC, followed by an obvious transition at 13:00 UTC,
542 opposite to that of ARPEGE-SH at 12:00 UTC. The warm and wet atmosphere observed after
543 13:00 UTC develops a mixed layer, consequently the PBL top no longer collapses to a stable
544 layer, in contrast to what was observed on 24 December. Furthermore, the SLW clouds present
545 in the entrainment zone steadily remain at the PBL top until the end of the day.

546

547 **5.3. Potential Temperature Gradient**

548 Figure 13 shows $\partial\theta/\partial z$ (K km^{-1}) from ARPEGE-SH, with the evolution of the PBL top and
549 the SLW cloud superimposed. In these perturbed conditions, the SLW clouds are present a few
550 tens of meters above the top of the PBL after 12:00 UTC. The PBL top is located in a layer
551 coinciding with the local maximum of $\partial\theta/\partial z$, around 100-300 m, and does not dramatically
552 decrease to the surface for the rest of the day.

553 Figures 14a, b and c show the vertical profiles of θ (K) and $\partial\theta/\partial z$ (K km^{-1}) as calculated
554 from temperature measured by the radiosondes and analysed by ARPEGE-SH at Dome C on
555 20 December 2018 at 00:00 and 12:00 UTC and on 21 December 2018 at 00:00 UTC,
556 respectively. The presence and the depth of the SLW cloud detected from LIDAR observations
557 are highlighted in the Figure. The ARPEGE-SH profiles are about 0-5 K warmer than the

558 observations. From 50 m upward, the maximum of $\partial\theta/\partial z$ is measured at 75, 150 and 375 m on
559 20 December 2018 at 00:00 and 12:00 UTC and on 21 December 2018 at 00:00 UTC,
560 respectively, with a corresponding amplitude of 75, 40 and 55 K km⁻¹. The location of the
561 observed maximum in the potential temperature gradient is consistent with the ARPEGE-SH
562 calculations on 20 December 2018 prior to the warm and wet episode: at 00:00 UTC (Fig. 14a),
563 the calculated $\partial\theta/\partial z$ is maximum at 75 m and reaches 100 K km⁻¹. However, at 12:00 UTC (Fig.
564 14b) the modelled $\partial\theta/\partial z$ peaks at 200 m (slightly higher than observed) with a value of 50 K
565 km⁻¹. On the following day at 00:00 UTC (Fig. 14c), $\partial\theta/\partial z$ calculated by ARPEGE-SH shows
566 two maxima at 100 and 450 m with an amplitude of 45 and 25 K km⁻¹, respectively, while the
567 observations demonstrate a single maximum just below 400 m.

568

569 **6. Impact of SLW Clouds on Net Surface Radiation**

570 The presence of clouds over Dome C has a strong impact on the net surface radiation as
571 demonstrated by Ricaud et al. (2017). This can be seen clearly in the time-series of upwelling
572 and downwelling longwave and shortwave fluxes observed by BSRN for the two case studies.

573

574 **6.1 Typical PBL Case – 24 December 2018**

575 Figure 15 (top) shows the time evolution of the net surface radiation as measured by the
576 BSRN instruments and as calculated by ARPEGE-SH on 24 December 2018, superimposed
577 with SLW cloud height. We also show the time evolution of the difference between surface
578 radiation (W m⁻²) observed by BSRN and calculated by ARPEGE-SH on 24 December 2018,
579 in longwave downward (LW↓), longwave upward (LW↑), shortwave downward (SW↓) and
580 shortwave upward (SW↑) components, superimposed with LWP. We highlight 4 periods with
581 images taken from the webcam installed on the shelter hosting the LIDAR and HAMSTRAD:
582 a) at 00:25 UTC (cirrus clouds, no SLW cloud), b) at 03:56 UTC (cirrus clouds, no SLW cloud),

583 c) at 09:46 UTC (SLW cloud) and d) at 17:20 UTC (SLW cloud). The net surface radiation
584 shows maxima between 00:00 and 05:00 UTC (08:00-13:00 LT) and minima between 11:00
585 and 13:00 UTC (19:00-21:00 LT) in the ARPEGE-SH and BSRN time series. When SLW
586 clouds are present in the observations (08:00-10:00, 12:00-19:00 and around 21:00 UTC),
587 whilst absent in ARPEGE-SH, the measured net surface radiation is systematically greater than
588 the simulated one by 20-30 W m^{-2} . In the presence of SLW clouds after 12:00 UTC, this
589 difference is mainly attributable to $\text{LW}\downarrow$ component, BSRN values being 50 W m^{-2} greater than
590 those of ARPEGE-SH. Thus, SLW clouds tend to radiate more LW radiation toward the ground
591 (like greenhouse gases) than more transparent clouds, like cirrus, do. There are differences from
592 -30 to +60 W m^{-2} between observed and calculated $\text{SW}\downarrow$ and $\text{SW}\uparrow$ components but this
593 difference falls within $\pm 10 \text{ W m}^{-2}$ for the net SW surface radiation ($\text{SW}\downarrow - \text{SW}\uparrow$). The reflective
594 impact of SLW layers can also be seen after 12:00 UTC: unlike observed SLW clouds,
595 ARPEGE-SH simulates ice clouds, and therefore too high $\text{SW}\downarrow$ values. The difference between
596 observed and simulated values of this parameter thus increases, as can be seen on the Figure.
597 But because of the high values in surface albedo, a compensating effect occurs on the surface
598 reflected SW fluxes, and the resulting impact on net radiation is quite weak (the time series of
599 the observed – simulated difference in incoming and reflected SW flux follow each other quite
600 well). The major impact on net radiation is therefore related to the longwave fluxes.

601

602 **6.2 Perturbed PBL Case – 20 December 2018**

603 Figure 16 (top) shows the net surface radiation as measured by the BSRN photometric
604 instruments and as calculated by ARPEGE-SH for 20 December 2018, superimposed with the
605 SLW clouds. We also show the time evolution of difference in surface radiation (W m^{-2})
606 observed by BSRN and calculated by ARPEGE-SH on 20 December 2018 for $\text{LW}\downarrow$, $\text{LW}\uparrow$,
607 $\text{SW}\downarrow$ and $\text{SW}\uparrow$ components, superimposed with LWP. We highlight 4 periods with snapshots

608 taken from the webcam: 1) 07:15 UTC (clear sky), 2) 12:35 UTC (clear sky), 3) 13:30 UTC
609 (SLW cloud) and 4) 21:00 UTC (SLW cloud). Before 13:00 UTC, there are no clouds above
610 Dome C whilst after 13:00 UTC clouds are present. The diurnal evolution of the modelled and
611 observed net surface radiation shows a maximum of $\sim+50 \text{ W m}^{-2}$ in ARPEGE-SH and $\sim+85 \text{ W}$
612 m^{-2} in BSRN over the period 00:00-04:00 UTC, and a minimum of about -50 W m^{-2} around
613 12:00-13:00 UTC on both time series. Nevertheless, when SLW clouds are observed at 13:00
614 UTC, the observed net surface radiation jumps to $+10 \text{ W m}^{-2}$, a feature not reproduced in the
615 model. The difference between the BSRN-observed and ARPEGE-SH-modelled net surface
616 radiation is larger than $+30 \text{ W m}^{-2}$ when SLW clouds are present, reaching $+60 \text{ W m}^{-2}$ when the
617 LWP measured by HAMSTRAD is at its maximum (50 g m^{-2} at 13:00 UTC). This is twice the
618 difference observed in the non-perturbed PBL episode detailed in section 3.4. This underlines
619 again the strong impact SLW clouds may have on the radiation budget over Antarctica. In the
620 presence of SLW clouds after 13:00 UTC, the difference in net surface radiation is mainly
621 attributable to $\text{LW}\downarrow$ component, BSRN values being 100 W m^{-2} greater than those of ARPEGE-
622 SH. The $\text{SW}\downarrow$ and $\text{SW}\uparrow$ also decrease due to the high reflectivity of the SLW layer seen at
623 12:00 UTC and again at 15:00 UTC. Note that there are differences from -100 to $+60 \text{ W m}^{-2}$
624 between observed and calculated $\text{SW}\downarrow$ and $\text{SW}\uparrow$ components but this difference falls below 20
625 W m^{-2} for the net SW surface radiation ($\text{SW}\downarrow - \text{SW}\uparrow$). Both SW components decrease after
626 17:00 UTC. Some of this may be due to: 1) increasing LWP, and 2) the presence of precipitating
627 ice crystals and/or blowing snow (characterized by red spots on Figure 9b) that are increasing
628 optical depth and decreasing transmission/visibility (webcam images in Figure 16d) although
629 surface wind was rather weak ($3\text{-}10 \text{ m s}^{-1}$, not shown).

630

631 **7. Discussions**

632 **7.1. SLW Clouds vs Mixed-Phase Clouds**

633 In order to evaluate whether the observed cloud is constituted of liquid and/or mixed phase
634 water, we have considered the raw signals recorded by the LIDAR. For the two dates under
635 consideration (Figures Supp8 and Supp9 relative to 24 and 20 December 2018, respectively),
636 we have represented (top) the P signal as the signal received with the same polarization as the
637 laser (unpolarized component). Any suspended object can contribute to P signal. We have also
638 represented the S (cross-polarized) LIDAR signal (bottom) that is only produced by non-
639 spherical (obviously frozen at Dome C) particles and, to a smaller extent, by multiple scattering
640 in water clouds.

641 First of all, an elevated P signal above ~400 m on 24 December 2018 ($P \geq 0.1$ mV) and
642 above ~200 m on 20 December 2018 ($P \geq 0.3$ mV) is associated with a cloud as shown in
643 sections 4.1 and 5.1. Inside these clouds, the S signal is always very low: $S \sim 0.003$ mV on 24
644 December 2018 and ~ 0.01 mV on 20 December 2018. Consequently, the S signal is very weak
645 and corresponds to a maximum of ~3% of the corresponding P signal. Some S signal is
646 nevertheless present in the cloud and could be given by multiple scattering inside the truly liquid
647 water cloud and/or the effective presence of ice particles.

648 When considering the LIDAR depolarization diurnal evolutions presented in Figures 2b
649 and 9b associated to the two dates, ice particles could have been disappeared in the low
650 depolarization ratio S/P of the SLW layer because the P signal inside the SLW cloud is very
651 high compared to the S signal. But when considering the P and S signals distinctively (Figs.
652 Supp8 and Supp9), the S signal remains very weak in the SLW cloud compared to the P signal
653 whatever the date considered. Consequently, even if the presence of some ice particles scattered
654 within the SLW layers cannot be excluded from the S signal plot, the very low depolarization
655 of the layers leads to classify them as a liquid cloud.

656 The important point is that the optical properties of the layer, relevant for the radiative
657 budget in the shortwave, such as optical extinction, optical depth, asymmetry factors, etc. are

658 bound to the P signal, being e.g. optical extinction in the visible proportional to the lidar P
659 signal. Thus, the shortwave radiative characteristics of the cloud are driven by the P signal, and
660 thus by liquid water.

661 On the other hand, when we consider the aerosol depolarization ratio measured by the
662 LIDAR (Figure 2b) and the total snow flux calculated by ARPEGE-SH (Figure Supp2) on 24
663 December 2018, it is obvious that solid precipitation is present from 00:00 to 10:00 UTC in a
664 layer from ~500 m to the surface (vertical stripes). Therefore, physical processes are occurring
665 within the cloud to deplete liquid and turn it into solid, causing the ice observed and calculated
666 below the SLW layer. In this case, the ice microphysics would also be important since it leads
667 to the termination of the SLW layer, hence indirectly impacting the radiative budget. As a
668 consequence, we cannot completely rule out the possibility that this is a SLW layer of an overall
669 mixed-phase cloud.

670

671 **7.2. SLW Clouds and PBL**

672 During the YOPP SOP-SH, SLW clouds were observed in the LIDAR data for 15 days in
673 December (49% of days) and 13 days in January (47%), which is a similar rate of occurrence
674 to other years (53% in December 2016 and 2018; 51% in January 2018 and 2019) (Figure 17).
675 A day is flagged with a SLW cloud occurrence when a SLW cloud has been detected in the
676 LIDAR observations for a period longer than 1 hour. The clouds observed during the SOP-SH
677 are typically located at the top of the PBL (100 to 400 m height) and are 50-100 m thick.

678 The presence of SLW clouds in the atmosphere is strongly dependent on the temperature
679 field. From Fig. 2.33 of Pruppacher and Klett (2012), the percentage of clouds containing no
680 ice becomes non-negligible at temperatures greater than -35°C , although SLW clouds have been
681 observed at lower temperatures over Russia (-36°C) and the Rocky Mountains in the USA (-

682 40.7°C). Recent laboratory measurements show that liquid water can exist down to -42.55°C
683 (Goy et al., 2018).

684 Considering that the SLW clouds at Dome C are so thin, they resemble stratocumulus, as
685 can be observed at middle latitudes. The diurnal cycle of the SLW cloud also evokes that of
686 oceanic stratocumulus, with a trend to fragmentation and/or dissipation during the “day” (local
687 noon) because of solar absorption and to a solid deck state during the “night” (local midnight)
688 because of reversed buoyancy due to cloud top longwave cooling. We use here the “night” and
689 “day” terms for convenience, though solar radiation remains positive 24-hr long at this period
690 of the year. During the SOP-SH, SLW clouds were observed in the LIDAR data for
691 approximately 48% of days (Fig. 17) but it is not yet evident whether they were formed during
692 the “day” (local noon) when the mixed layer becomes thick enough to reach the condensation
693 level, and vertically broadened during the “night”, or created during the “night” (local midnight)
694 and then dissipated during the coming “day”. Complementary observations would be needed,
695 in particular turbulence profiles from the surface to above the top of boundary-layer clouds, to
696 determine what is the coupling/decoupling diurnal cycle of these clouds.

697 The diurnal evolution of the top of the PBL is consistent with previous studies carried out
698 at Dome C (e.g. Argentini et al., 2005; King et al., 2006; Ricaud et al., 2012; Casasanta et al.,
699 2014), with a top higher when there is a relatively warm mixed layer than in colder stable
700 conditions.

701 The collocation of the positive potential temperature gradient with the height of the SLW
702 clouds is consistent with the schematic representation of the diurnal variation of the PBL
703 illustrated by Stull (2012) and adapted by Ricaud et al. (2012) for the Eastern Antarctic Plateau.
704 Figure 18 is a modified version of Figure 12 from Ricaud et al. (2012) to take into account the
705 impact of the clouds on the PBL structure. Starting with the simplest, cloud-free case, we have
706 during the convective (mixing) period a mixed layer at the top of which is located the

707 “entrainment zone”, so-named because air parcels coming from the above free troposphere are
708 entrained into the mixed layer below under the effect of overshooting thermals and
709 compensating descending currents. When clouds form at the top of the PBL (boundary-layer
710 clouds), we consider that the PBL locally (i.e. where clouds are present) extends to the top of
711 these clouds. The PBL is clearly separated from the above stable free troposphere by the so-
712 called “capping inversion”. The cloud layers as well as the capping inversion zone are thin, of
713 the order of 100 m. When the stable layer forms close to the surface, the SLW cloud may persist
714 over the residual mixed layer, as may persist the capping inversion zone which can also be
715 qualified as “residual”. The stable layer is then progressively eroded, when the incoming
716 available energy becomes large enough to ensure turbulent mixing from the surface. The new
717 mixing layer thus grows through the previous stable layer and residual mixed layer, up to it
718 reaches the residual capping inversion. The stratification of the different layers is characterized
719 by the simplified potential temperature profiles in Figure 18. Considering both the potential
720 temperature gradients and the vertical extent of the SLW cloud, these layers are quite thin, less
721 than 100-m deep.

722

723 **7.3 SLW Clouds in ARPEGE-SH**

724 In comparison with observations, ARPEGE-SH consistently underestimates LWP by
725 several orders of magnitude. This is due in part to the partitioning into liquid and ice phases in
726 the model which is a simple function of temperature such that, below -20°C , all cloud particles
727 are iced. The inability of ARPEGE-SH to reproduce the observed liquid water content of the
728 cloud leads to an underestimate of the simulated downwelling longwave radiation relative to
729 observations, and an overestimate of both upwelling and downwelling shortwave flux. This
730 effect is particularly notable in the perturbed PBL case study where the high moisture content
731 leads to an enhanced longwave effect. As the SLW cloud horizontal extent in the first case

732 study is between ~450 and ~700 km and persists over more than 12 hours (section 4.1), the
733 discrepancy in the net surface radiation between observation and NWP model may have a strong
734 impact on the calculation of the radiation budget over Antarctica. Lawson and Gettelman (2014)
735 showed that better representation of liquid water in modelled mixed phase clouds in Global
736 Climate Models led to an increase of 7.4 W m^{-2} in the cloud radiative effect over Antarctica.

737 In Figure 17, we show the percentage of days per month that SLW clouds were detected
738 within the LIDAR data for more than 12 hours per day (blue) during SOP-SH. As expected,
739 SLW clouds with a minimum duration of 12 hours (blue) occur less often than SLW clouds
740 with a minimum duration of 1 hour (green). But, whatever the criterium used (1 hour or 12
741 hours), the maxima of SLW cloud presence occur in December and January during SOP-SH.
742 12-h SLW clouds occurred about a quarter of the days (20-25%) compared to roughly half of
743 the days for 1-h SLW clouds (40-45%). This reinforces the argument of the critical importance
744 of well representing SLW clouds in models in order to better estimate radiation budget over
745 Antarctica.

746 Furthermore, even when considering analyses of ARPEGE-SH at 00:00, 06:00, 12:00 and
747 18:00 UTC and associated forecasts (not shown), neither IVW nor LWP are significantly
748 modified, and SLW remains underestimated. The 4Dvar analysis is not able to correct the dry
749 bias especially during the case of 20 December 2018 probably because it is influenced by a
750 large-scale advection. The underestimation of the SLW in ARPEGE-SH can be explained by
751 the fact that: 1) the underestimation of liquid water is mainly a physical problem in the model
752 related to the ice/liquid partition function vs temperature (see below) and 2), since the cloud
753 water is not a model control variable in the 4DVar scheme, it cannot be updated by the analysis
754 step of the 4DVar data assimilation process.

755 We have thus tried to modify the ice partition function (ice/liquid water vs temperature)
756 used in the ARPEGE-SH operational model (Figure Supp10). We noticed that, for temperatures

757 below -20°C , water was present only in the solid form in the model. A test has been performed
758 for 20 and 24 December 2018 with ARPEGE-SH by considering a new ice partition function
759 allowing the presence of liquid water for temperature between -20°C and -40°C (Figure
760 Supp10). The analyses were done at 00:00 UTC and the forecasts from 01:00 to 24:00 UTC.
761 This run was labelled as ARPEGE-SH-TEST.

762 For 24 December 2018, and consistently with Fig. 3, we have drawn on Fig. Supp11 the
763 diurnal evolutions of different variables calculated by ARPEGE-SH-TEST: a) the Cloud
764 Fraction, b) the Ice Water mixing ratio and c) the Liquid Water mixing ratio. Similarly, and
765 consistently with Fig. 4, Figure 19 presents: a) the ARPEGE-SH-TEST TCI, b) the LWP
766 measured by HAMSTRAD and calculated by ARPEGE-SH-TEST and c) the IWV measured
767 by HAMSTRAD and calculated by ARPEGE-SH-TEST. Eventually, and consistently with Fig.
768 9, Figure Supp13 presents the net surface radiation observed by BSRN and calculated by
769 ARPEGE-SH-TEST, and the difference between surface radiation of longwave downward,
770 longwave upward, shortwave downward and shortwave upward components observed by
771 BSRN and calculated by ARPEGE-SH-TEST. In the same manner, for the case of 20 December
772 2018, Figs. Supp12, 20 and Supp14 echo Figs. 11, 12 and 16, respectively.

773 On 24 December 2018 (typical case), the new partition function significantly improves the
774 modelled SLW, with liquid water content about 1000 times greater in ARPEGE-SH-TEST than
775 in ARPEGE-SH, and LWP varying from ~ 0 to $\sim 3 \text{ g m}^{-2}$ consistently with HAMSTRAD to
776 within $\pm 0.5 \text{ g m}^{-2}$. The impact on the net surface radiation is obvious with an excellent
777 agreement between ARPEGE-SH-TEST and BSRN to within $\pm 20 \text{ W m}^{-2}$. Unfortunately, on
778 20 December 2018 (perturbed case), even if the impact on SWL clouds is important (liquid
779 water content multiplied by a factor 100), LWP is still a factor 10 less in ARPEGE-SH-TEST
780 than in HAMSTRAD. ARPEGE-SH-TEST still fails to reproduce the large increase in liquid
781 water and IWV at 13:00 UTC since the local maximum is calculated 2 hours later. The impact

782 on the net surface radiation is weak with ARPEGE-SH-TEST underestimating the net surface
783 radiation by 50 W m^{-2} compared to observations, mainly attributable to the downwelling
784 longwave surface radiation from BSRN being 100 W m^{-2} greater than that of ARPEGE-SH-
785 TEST.

786 Finally, the bias on the net surface radiation and the underestimation of IWV and LWP of
787 the model compared to the observations is strongly reduced when using a new ice partition
788 function in ARPEGE-SH-TEST. This suggests that LWP has more impact than IWV on $\text{LW}\downarrow$
789 due to the small quantities of specific humidity at Dome C.

790

791 **8. Conclusions**

792 A comprehensive water budget study has been performed during the Year of Polar Programs
793 SOP-SH at Dome C (Concordia, Antarctica) from mid-November 2018 to mid-February 2019.
794 Supercooled liquid water (SLW) clouds were observed and analysed by means of remote-
795 sensing ground-based instrumentation (tropospheric depolarization LIDAR, HAMSTRAD
796 microwave radiometer, BSRN net surface radiation), radiosondes, spaceborne sensor
797 (CALIOP/CALIPSO depolarization LIDAR) and the NWP ARPEGE-SH. The analysis shows
798 that SLW clouds were present from November to March, with the greatest frequency occurring
799 in December and January since $\sim 50\%$ of the days in summer time exhibited SLW clouds for at
800 least one hour. The clouds observed during the SOP-SH are typically located at the top of the
801 boundary layer (100 to 400 m height) and are 50-100 m thick.

802 The analyses focused on two periods showing 1) a typical diurnal cycle of the PBL on 24
803 December 2018 (warm and dry, local mixing layer followed by a thinner cold and dry, local
804 stable layer which develops when the surface has cooled down) and 2) a perturbed diurnal cycle
805 of the PBL on 20 December 2018 (a warm and wet episode prevented from a clear diurnal cycle
806 of the PBL top). In both cases thin ($\sim 100\text{-m}$ thick) SLW clouds have been observed by ground-

807 based and spaceborne LIDARs developing within the entrainment and the capping inversion
808 zones at the top of the PBL. Spaceborne LIDAR observations revealed horizontal extensions of
809 these clouds as large as 700 km for the 24 December case study. ARPEGE-SH was not able to
810 correctly estimate the ratio between liquid and solid water inside the cloudy layers, with SLW
811 always strongly underestimated by a factor 1000 in the studied cases, mainly because the
812 liquid/ice partition function used in the model favours ice at temperatures less than -20°C .
813 Consequently, the net surface radiation was affected by the presence of SLW clouds during
814 these two episodes. The net surface radiation observed by BSRN was $20\text{-}30\text{ W m}^{-2}$ higher than
815 that modelled in ARPEGE-SH on 24 December 2018 (typical diurnal cycle of the PBL), this
816 difference reaching $+50\text{ W m}^{-2}$ on 20 December 2018 (perturbed diurnal cycle of the PBL),
817 consistent with the total observed liquid water being 20 times greater in the perturbed PBL
818 diurnal cycle than in the typical PBL diurnal cycle. The difference in the net surface radiation
819 is mainly attributable to longwave downward surface radiation, BSRN values being 50 and 100
820 W m^{-2} greater than those of ARPEGE-SH in the typical and perturbed cases, respectively.

821 The ice/liquid partition function used in the ARPEGE-SH NWP has been modified to favour
822 liquid water at temperatures below -20°C down to -40°C . For the two study cases, the model
823 run with this new partition function has been able to generate SLW clouds. During the typical
824 case, modelled LWP was consistent with observations and, consequently, the net surface
825 radiation calculated by the model agreed with measurements to within $\pm 20\text{ W m}^{-2}$. During the
826 perturbed case, modelled LWP was a factor 10 less than observations and, consequently, the
827 model underestimated the net surface radiation by $\sim 50\text{ W m}^{-2}$ compared to observations.

828 Time coincident ground-based remote-sensed measurements of water (vapour, liquid and
829 solid), temperature and net surface radiation are available at Dome C since 2015. Consequently,
830 a comprehensive statistical analysis of the presence of SLW clouds will be performed in the

831 near future. Coupled with modelling studies (NWP ARPEGE-SH, mesoscale models), an
832 estimation of the radiative impact of these clouds on the local climate will then be performed.

833

834 **Data availability**

835 HAMSTRAD data are available at <http://www.cnrm.meteo.fr/spip.php?article961&lang=en>
836 (last access: 28 August 2019). The CALIOP images are accessible at [http://www-](http://www-calipso.larc.nasa.gov/)
837 [calipso.larc.nasa.gov/](http://www-calipso.larc.nasa.gov/) (last access: 28 August 2019). The tropospheric depolarization LIDAR
838 data are reachable at http://lidarmax.altervista.org/englidar/_Antarctic%20LIDAR.php (last
839 access: 28 August 2019). Radiosondes are available at <http://www.climantartide.it> (last access:
840 28 August 2019). BSRN data can be obtained from the ftp server ([https://bsrn.awi.de/data/data-](https://bsrn.awi.de/data/data-retrieval-via-ftp/)
841 [retrieval-via-ftp/](https://bsrn.awi.de/data/data-retrieval-via-ftp/)) (last access: 28 August 2019). The ARPEGE data and corresponding
842 technical information are available from the YOPP Data Portal and from the ftp server ([ftp.umr-](ftp.umr-cnrm.fr)
843 [cnrm.fr](ftp.umr-cnrm.fr) with user: yopp and password: Arpege) (last access: 28 August 2019). The NCEP data
844 are available at <https://www.esrl.noaa.gov/psd/> and the back-trajectory calculations can be
845 performed at <https://www.ready.noaa.gov/HYSPLIT.php>.

846

847 **Author contributions**

848 PR, MDG, AL, and PG provided the observational data while EB, NA and VG developed
849 the model code and performed the simulations. PD, JLA and DV contributed to the data
850 interpretation. All the co-authors participated in the data analysis. PR prepared the manuscript
851 with contributions from all co-authors. DV, EB, NA, MDG and PD also contributed
852 significantly to the revision of the manuscript supervised by PR.

853

854 **Competing interests**

855 The authors declare that they have no conflict of interest.

856

857 **Acknowledgments**

858 The present research project Water Budget over Dome C (H2O-DC) has been approved by
859 the Year of Polar Prediction (YOPP) international committee. The HAMSTRAD programme
860 (910) was supported by the French Polar Institute, Institut polaire français Paul-Emile Victor
861 (IPEV), the Institut National des Sciences de l'Univers (INSU)/Centre National de la Recherche
862 Scientifique (CNRS), Météo-France and the Centre National d'Etudes Spatiales (CNES). The
863 permanently manned Concordia station is jointly operated by IPEV and the Italian Programma
864 Nazionale Ricerche in Antartide (PNRA). The tropospheric LIDAR operates at Dome C from
865 2008 within the framework of several Italian national (PNRA) projects. We would like to thank
866 all the winterover personnel who worked at Dome C on the different projects: HAMSTRAD,
867 aerosol LIDAR and BSRN. The authors also acknowledge the CALIPSO science team for
868 providing the CALIOP images. We acknowledge the NCEP_Reanalysis 2 data provided by the
869 NOAA/OAR/ESRL PSD, Boulder, Colorado, USA, from their Web site at
870 <https://www.esrl.noaa.gov/psd/> and the NOAA Air Resources Laboratory to have accessed the
871 HYSPLIT model through <https://www.ready.noaa.gov/HYSPLIT.php>. We would like to thank
872 the two anonymous reviewers for their beneficial comments.

873

874 **References**

875 Adhikari, L., Wang, Z. and Deng, M.: Seasonal variations of Antarctic clouds observed by
876 CloudSat and CALIPSO satellites, *J. Geophys. Res.*, 117, D04202,
877 doi:10.1029/2011JD016719, 2012.

878 Argentini, S., Viola, A., Sempreviva, A. M. and Petenko, I.: Summer boundary-layer height at
879 the plateau site of Dome C, Antarctica, *Bound.-Layer Meteor.*, 115, 409-422, 2005.

880 Bromwich, D. H., Nicolas, J. P., Hines, K. M., Kay, J. E., Key, E. L., Lazzara, M. A., ... &
881 Lachlan-Cope, T. (2012). Tropospheric clouds in Antarctica. *Reviews of Geophysics*,
882 50(1).

883 Bromwich, D. H., Otieno, F. O., Hines, K. M., Manning, K. W., & Shilo, E. (2013).
884 Comprehensive evaluation of polar weather research and forecasting model performance in
885 the Antarctic. *Journal of Geophysical Research: Atmospheres*, 118(2), 274-292.

886 Casasanta, G., Pietroni, I., Petenko, I., and Argenti, S.: Observed and modelled convective
887 mixing-layer height at Dome C, Antarctica, *Boundary-layer meteorology*, 151(3), 597-608,
888 2014.

889 Driemel, A., Augustine, J., Behrens, K., Colle, S., Cox, C., Cuevas-Agulló, E., et al.: Baseline
890 Surface Radiation Network (BSRN): structure and data description (1992–2017), *Earth*
891 *Syst. Sci. Data*, 10, 1491-1501, <https://doi.org/10.5194/essd-10-1491-2018>, 2018.

892 Goy, C., Potenza, M. A., Deder, S., Tomut, M., Guillerm, E., Kalinin, A., ... and Tejada, G.:
893 Shrinking of rapidly evaporating water microdroplets reveals their extreme supercooling.
894 *Physical review letters*, 120(1), 015501, 2018.

895 Grazioli, J. and Genthon, C. and Boudevillain, B. and Duran-Alarcon, C. and Del Guasta, M.
896 and Madeleine, J.-B. and Berne, A.: Measurements of precipitation in Dumont d'Urville,
897 Adelie Land, East Antarctica, *The Cryosphere*, 11(4), 1797-1811, 2017.

898 Grosvenor, D. P., Choularton, T. W., Lachlan-Cope, T., Gallagher, M. W., Crosier, J., Bower,
899 K. N., Ladkin, R. S., and Dorsey, J. R.: In-situ aircraft observations of ice concentrations
900 within clouds over the Antarctic Peninsula and Larsen Ice Shelf, *Atmos. Chem. Phys.*, 12,
901 11275–11294, <https://doi.org/10.5194/acp-12-11275-2012>, 2012.

902 Hogan, R. J., and Illingworth, A. J.: The effect of specular reflection on spaceborne lidar
903 measurements of ice clouds. Report of the ESA Retrieval algorithm for EarthCARE project,
904 2003.

905 Kanamitsu, M. W. Ebisuzaki, J. Woollen, S-K Yang, J.J. Hnilo, M. Fiorino, and G. L. Potter.
906 NCEP-DOE AMIP-II Reanalysis (R-2), *Bulletin of the American Meteorological Society*,
907 1631-1643, Nov 2002. <https://doi.org/10.1175/BAMS-83-11-1631>.

908 King, J. C., Argentini, S. A., & Anderson, P. S. (2006). Contrasts between the summertime
909 surface energy balance and boundary layer structure at Dome C and Halley stations,
910 Antarctica. *Journal of Geophysical Research: Atmospheres*, 111(D2).

911 King, J. C., Gadian, A., Kirchgaessner, A., Kuipers Munneke, P., Lachlan-Cope, T. A., Orr, A.,
912 Reijmer, C., Broeke, M. R., van Wessem, J. M., and Weeks, M.: Validation of the
913 summertime surface energy budget of Larsen C Ice Shelf (Antarctica) as represented in
914 three high-resolution atmospheric models, *J. Geophys. Res.-Atmos.*, 120, 1335–1347,
915 <https://doi.org/10.1002/2014JD022604>, 2015.

916 Lachlan-Cope, T. (2010). Antarctic clouds. *Polar Research*, 29(2), 150-158.

917 Lachlan-Cope, T., Listowski, C., and O’Shea, S.: The microphysics of clouds over the Antarctic
918 Peninsula – Part 1: Observations, *Atmos. Chem. Phys.*, 16, 15605–15617,
919 <https://doi.org/10.5194/acp-16-15605-2016>, 2016.

920 Lawson, R. P., & Gettelman, A. (2014). Impact of Antarctic mixed-phase clouds on climate.
921 *Proceedings of the National Academy of Sciences*, 111(51), 18156-18161.

922 Legrand, M., Yang, X., Preunkert, S., and Therys, N.: Year-round records of sea salt, gaseous,
923 and particulate inorganic bromine in the atmospheric boundary layer at coastal (Dumont
924 d’Urville) and central (Concordia) East Antarctic sites, *J. Geophys. Res. Atmos.*, 121, 997–
925 1023, <https://doi.org/10.1002/2015JD024066>, 2016.

926 Listowski, C. and Lachlan-Cope, T.: The microphysics of clouds over the Antarctic Peninsula
927 – Part 2: modelling aspects within Polar WRF, *Atmos. Chem. Phys.*, 17, 10195–10221,
928 <https://doi.org/10.5194/acp-17-10195-2017>, 2017

929 Listowski, C., Delanoë, J., Kirchgaessner, A., Lachlan-Cope, T., and King, J.: Antarctic clouds,
930 supercooled liquid water and mixed-phase investigated with DARDAR: geographical and
931 seasonal variations, *Atmos. Chem. Phys.*, 19, 6771–6808, 2019.

932 Lubin, D., Chen, B., Bromwich, D. H., Somerville, R. C., Lee, W. H., and Hines, K. M.: The
933 Impact of Antarctic Cloud Radiative Properties on a GCM Climate Simulation, *J. Climate*,
934 11, 447-462, 1998.

935 Miloshevich, L. M., Vömel, H., Whiteman, D. N., Lesht, B. M., Schmidlin, F. J., and Russo,
936 F.: Absolute accuracy of water vapor measurements from six operational radiosonde types
937 launched during AWEX-G and implications for AIRS validation, *J. Geophys. Res.*, 111,
938 D09S10, doi:10.1029/2005JD006083, 2006.

939 Miloshevich, L. M., Vömel, H., Whiteman, D. N., and Leblanc, T.: Accuracy assessment and
940 corrections of Vaisala RS92 radiosonde water vapour measurements, *J. Geophys. Res.*, 114,
941 D11305, doi:10.1029/2008JD011565, 2009.

942 Mishchenko, M. I., J. W. Hovenier, and L. D. Travis (Eds.): *Light Scattering by Nonspherical*
943 *Particles: Theory, Measurements, and Applications*. Academic Press. Chapter 14, 393-416,
944 2000.

945 O’Shea, S. J., Choularton, T. W., Flynn, M., Bower, K. N., Gallagher, M., Crosier, J., Williams,
946 P., Crawford, I., Fleming, Z. L., Listowski, C., Kirchgaessner, A., Ladkin, R. S., and
947 Lachlan-Cope, T.: In situ measurements of cloud microphysics and aerosol over coastal
948 Antarctica during the MAC campaign, *Atmos. Chem. Phys.*, 17, 13049–13070,
949 <https://doi.org/10.5194/acp-17-13049-2017>, 2017.

950 Pailleux, J., Geleyn, J.-F., El Khatib, R., Fischer, C., Hamrud, M., Thépaut, J.-N., et al. (2015).
951 Les 25 ans du système de prévision numérique du temps IFS/Arpège, *La Météorologie*, 89,
952 18-27, <http://hdl.handle.net/2042/56594>, DOI : <https://doi.org/10.4267/2042/56594>

953 Palchetti, L., Bianchini, G., Di Natale, G., and Del Guasta, M.: Far infrared radiative properties
954 of water vapor and clouds in Antarctica, *B. Am. Meteorol. Soc.*, 96, 1505-1518,
955 doi:10.1175/BAMS-D-13-00286.1, 2015.

956 Pruppacher, H. R., and Klett, J. D.: *Microphysics of Clouds and Precipitation*: Reprinted 1980.
957 Springer Science & Business Media, Second revised and enlarged edition, 2012.

958 Ricaud, P., Gabard, B., Derrien, S., Chaboureau, J.-P., Rose, T., Mombauer, A. and Czekala,
959 H.: HAMSTRAD-Tropo, A 183-GHz Radiometer Dedicated to Sound Tropospheric Water
960 Vapor Over Concordia Station, Antarctica, *IEEE Trans Geosci Remote Sens.*, 48, 1365–
961 1380, doi: 10.1109/TGRS.2009.2029345, 2010a.

962 Ricaud, P., B., Gabard, S. Derrien, J.-L. Attié, T. Rose, and H. Czekala, Validation of
963 tropospheric water vapor as measured by the 183-GHz HAMSTRAD Radiometer over the
964 Pyrenees Mountains, France, *IEEE Transactions on Geoscience and Remote Sensing*, Vol.
965 48, No. 5, 2189-2203, 2010b.

966 Ricaud, P., Genthon, C., Durand, P., Attié, J.-L., Carminati, F., Canut, G., Vanacker, J.-F.,
967 Moggio, L., Courcoux, Y., Pellegrini, A. and Rose, T.: Summer to Winter Diurnal
968 Variabilities of Temperature and Water Vapor in the lowermost troposphere as observed by
969 the HAMSTRAD Radiometer over Dome C, Antarctica, *Bound.-Layer Meteor.*, 143, 227–
970 259, doi:10.1007/s10546-011-9673-6, 2012.

971 Ricaud, P., Grigioni, P., Zbinden, R., Attié, J.-L., Genoni, L., Galeandro, A., Moggio, A.,
972 Montaguti, S., Petenko, I. and Legovini, P.: Review of tropospheric temperature, absolute
973 humidity and integrated water vapour from the HAMSTRAD radiometer installed at Dome
974 C, Antarctica, 2009–14, *Antarct. Sci.*, 27, 598-616, doi:10.1017/S0954102015000334,
975 2015.

976 Ricaud, P., Bazile, E., del Guasta, M., Lanconelli, C., Grigioni, P., and Mahjoub, A.: Genesis
977 of diamond dust, ice fog and thick cloud episodes observed and modelled above Dome C,
978 Antarctica, *Atmos. Chem. Phys.*, 17, 5221-5237, doi:10.5194/acp-17-5221-2017, 2017.

979 Rolph, G., Stein, A., and Stunder, B., (2017). Real-time Environmental Applications and
980 Display sYstem: READY. *Environmental Modelling & Software*, 95, 210-228,
981 <https://doi.org/10.1016/j.envsoft.2017.06.025>.

982 Stein, A.F., Draxler, R.R, Rolph, G.D., Stunder, B.J.B., Cohen, M.D., and Ngan, F., (2015).
983 NOAA's HYSPLIT atmospheric transport and dispersion modeling system, *Bull. Amer.*
984 *Meteor. Soc.*, 96, 2059-2077, <http://dx.doi.org/10.1175/BAMS-D-14-00110.1>.

985 Stull, R. B.: An introduction to boundary layer meteorology (Vol. 13). Springer Science &
986 Business Media, 2012.

987 Tomasi, C., Petkov, B., Mazzola, M., Ritter, C., di Sarra, A., di Iorio, T., and del Guasta, M.:
988 Seasonal variations of the relative optical air mass function for background aerosol and thin
989 cirrus clouds at Arctic and Antarctic sites, *Remote Sensing*, 7(6), 7157-7180, 2015.

990 Winker, D. M., Vaughan, M. A., Omar, A., Hu, Y., Powell, K. A., Liu, Z., Hunt, W. H. and
991 Young, S. A.: Overview of the CALIPSO mission and CALIOP data processing algorithms,
992 *J. Atmos. Oceanic Technol.*, 26, 2310-2323, 2009.

993 Young, S. A. and Vaughan, M. A.: The retrieval of profiles of particulate extinction from Cloud
994 Aerosol Lidar Infrared Pathfinder Satellite Observations (CALIPSO) lidar data: Algorithm
995 description, *J. Atmos. Oceanic Technol.*, 26, 1105–1119, 2009.

996 Young, G., Lachlan-Cope, T., O'Shea, S. J., Dearden, C., Listowski, C., Bower, K. N., et al.
997 Radiative effects of secondary ice enhancement in coastal Antarctic clouds. *Geophysical*
998 *Research Letters*, 46. doi:10.1029/2018GL080551, 2019.

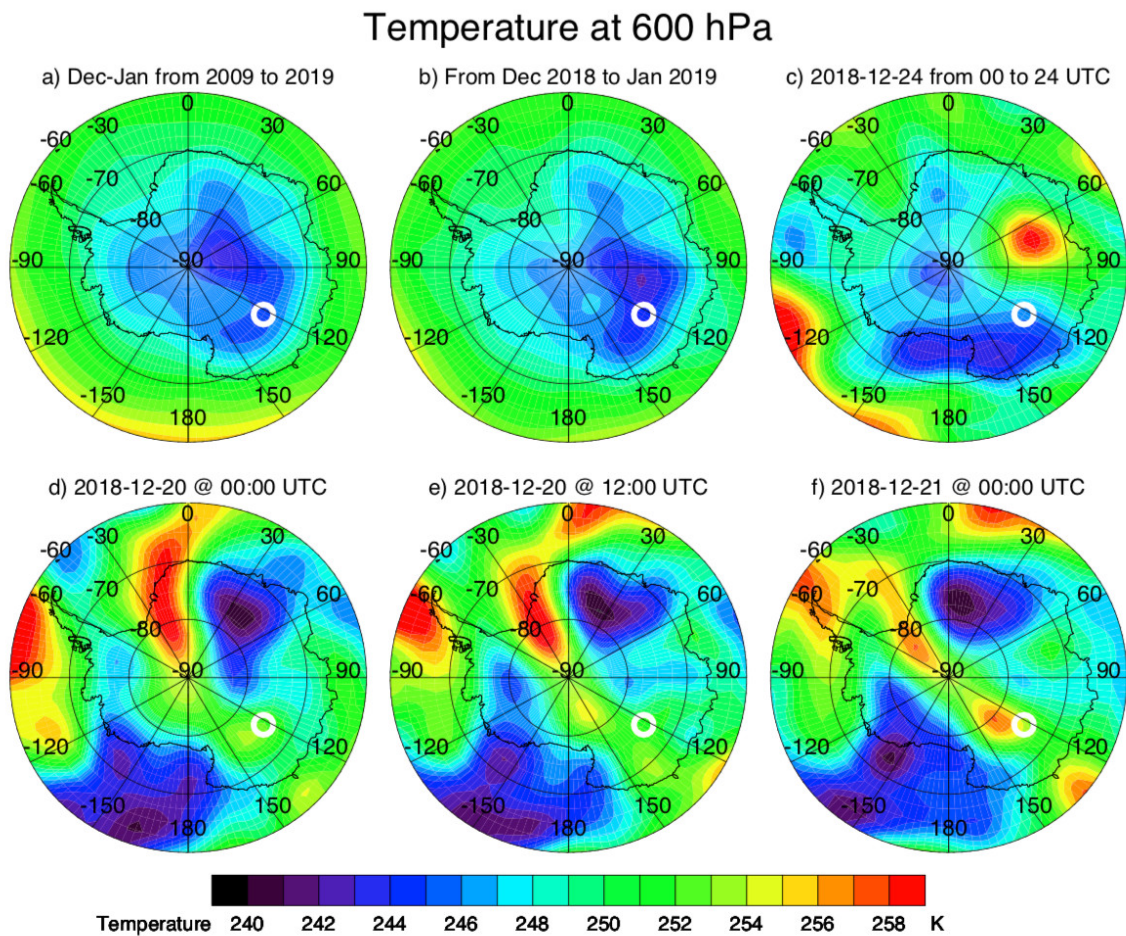
999 Young, G. and Jones, H. M. and Choularton, T. W. and Crosier, J. and Bower, K. N. and
1000 Gallagher, M. W. and Davies, R. S. and Renfrew, I. A. and Elvidge, A. D. and Darbyshire,

1001 E. and Marengo, F. and Brown, P. R. A. and Ricketts, H. M. A. and Connolly, P. J. and
1002 Lloyd, G. and Williams, P. I. and Allan, J. D. and Taylor, J. W. and Liu, D. and Flynn, M.
1003 J.: Observed microphysical changes in Arctic mixed-phase clouds when transitioning from
1004 sea ice to open ocean, *Atmos. Chem. Phys.*, 16(21), 13945-13967, doi:10.5194/acp-16-
1005 13945-2016, 2016.
1006
1007

1008

Figures

1009

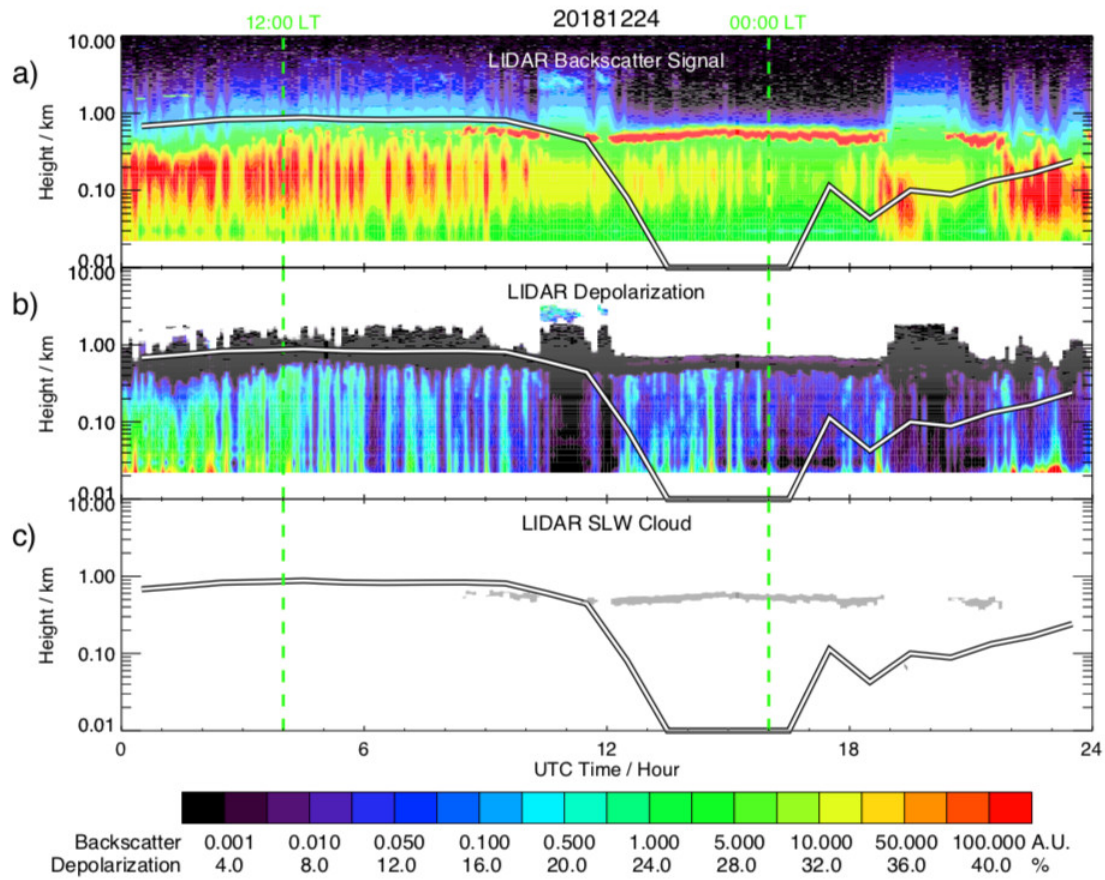


1010

1011 **Figure 1:** Temperature fields from NCEP at 600 hPa: a) decadal average over December-
1012 January from 2009 to 2019, b) YOPP average over December 2018-January 2019, c) daily
1013 average over 24 December 2018, d) 20 December 2018 at 00:00 UTC, e) 20 December 2018 at
1014 12:00 UTC, and f) 21 December 2018 at 00:00 UTC. The white circle represents the position
1015 of the Dome C station.

1016

1017

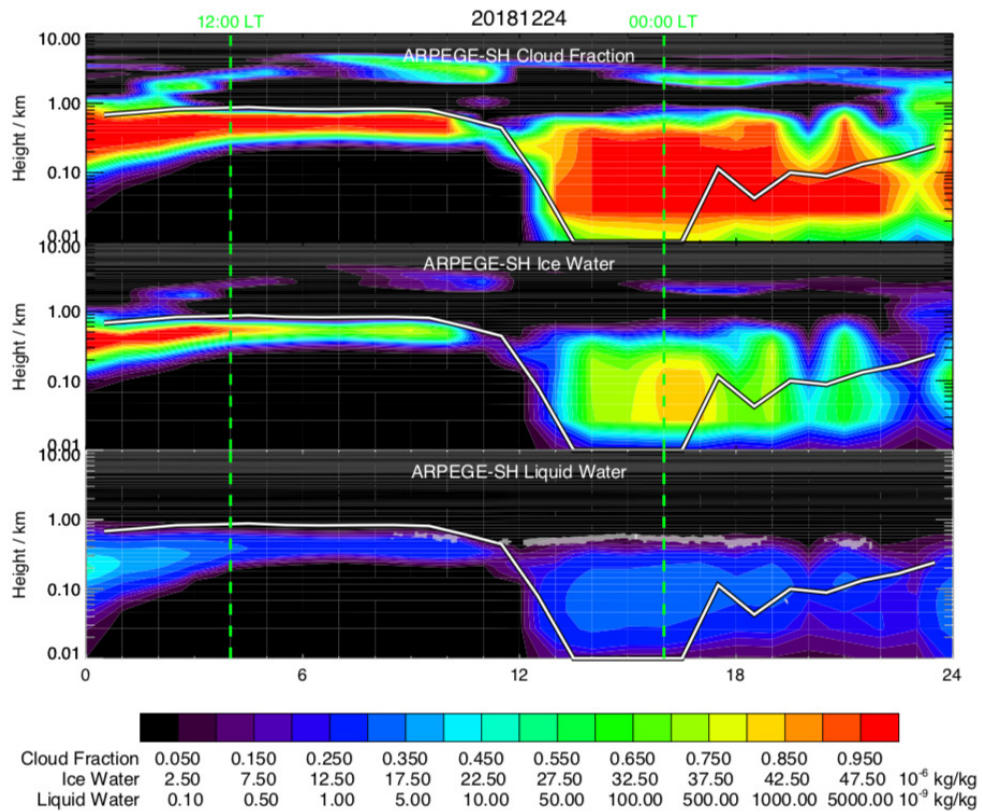


1018

1019 **Figure 2:** Diurnal variation on 24 December 2018 (UTC Time) along the vertical of: a) the
 1020 backscatter signal (Arbitrary Unit, A.U.), b) the depolarization ratio (%) measured by the
 1021 aerosol LIDAR, and c) the Supercooled Liquid Water (SLW) cloud height (grey) deduced from
 1022 the aerosol LIDAR ($\beta_c > 100 \beta_{mol}$, depolarization $< 5\%$). Superimposed to all the Figures is the
 1023 top of the Planetary Boundary Layer calculated by the ARPEGE-SH model (black-white thick
 1024 line). Two vertical green dashed lines indicate 12:00 and 00:00 LT.

1025

1026

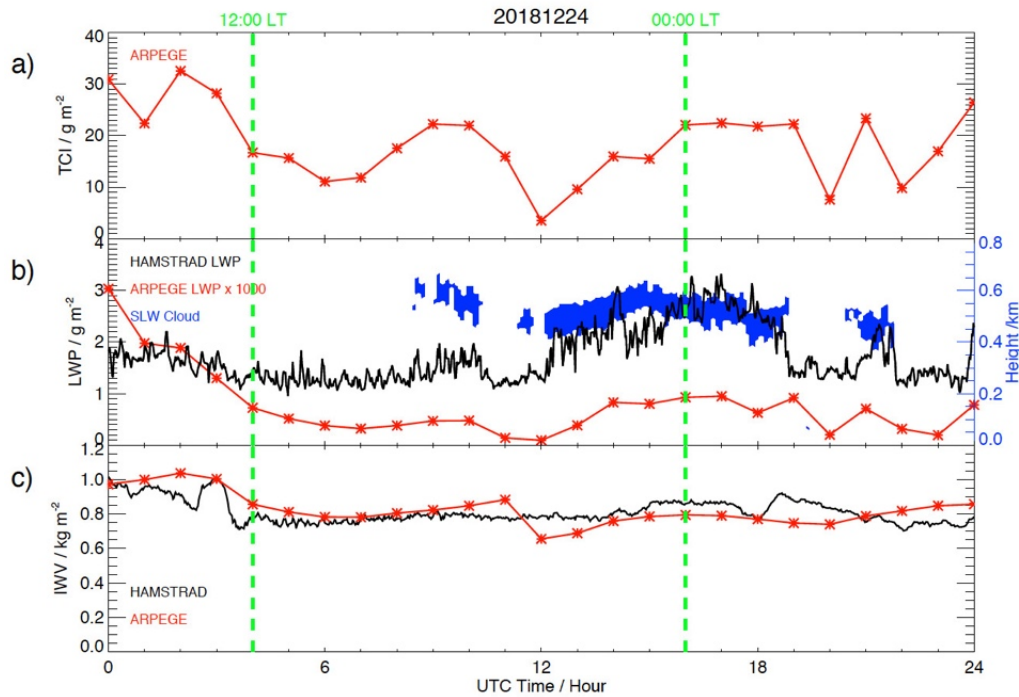


1027

1028 **Figure 3:** Time-height cross section on 24 December 2018 (UTC Time) of: a) the Cloud
1029 Fraction (0-1), b) the Ice Water mixing ratio (10^{-6} kg kg $^{-1}$) and c) the Liquid Water mixing ratio
1030 (10^{-9} kg kg $^{-1}$) calculated by the ARPEGE-SH model. Superimposed to all the panels is the top
1031 of the Planetary Boundary Layer calculated by the ARPEGE-SH model (black-white thick line).
1032 Superimposed in panel c is the SLW cloud (grey area) deduced from the LIDAR observations
1033 (see Fig. 1c). Two vertical green dashed lines indicate 12:00 and 00:00 LT.

1034

1035



1036

1037 **Figure 4:** Diurnal variation on 24 December 2018 (UTC Time) of: a) the Total Column of Ice

1038 (TCI) (g m^{-2}) calculated by ARPEGE-SH (red crossed line), b) the Liquid Water Path (LWP)

1039 measured by HAMSTRAD (g m^{-2} , black solid line) and calculated by ARPEGE-SH ($\times 1000 \text{ g}$

1040 m^{-2} , red crossed line) and c) the Integrated Water Vapour (IWV, kg m^{-2}) measured by

1041 HAMSTRAD (black solid line) and calculated by ARPEGE-SH (red crossed line).

1042 Superimposed to panel b) is the SLW cloud thickness (blue area) deduced from the LIDAR

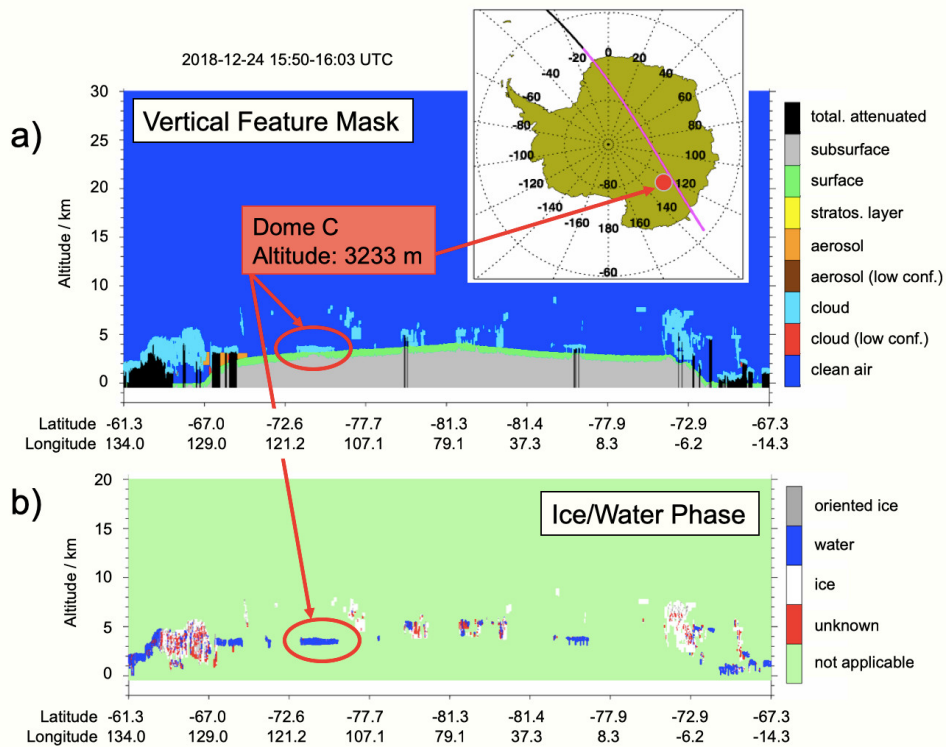
1043 observations (see Fig. 1c) (blue y-axis on the right of the Figure). Note LWP from ARPEGE-

1044 SH has been multiplied by a factor 1000. Two vertical green dashed lines indicate 12:00 and

1045 00:00 LT.

1046

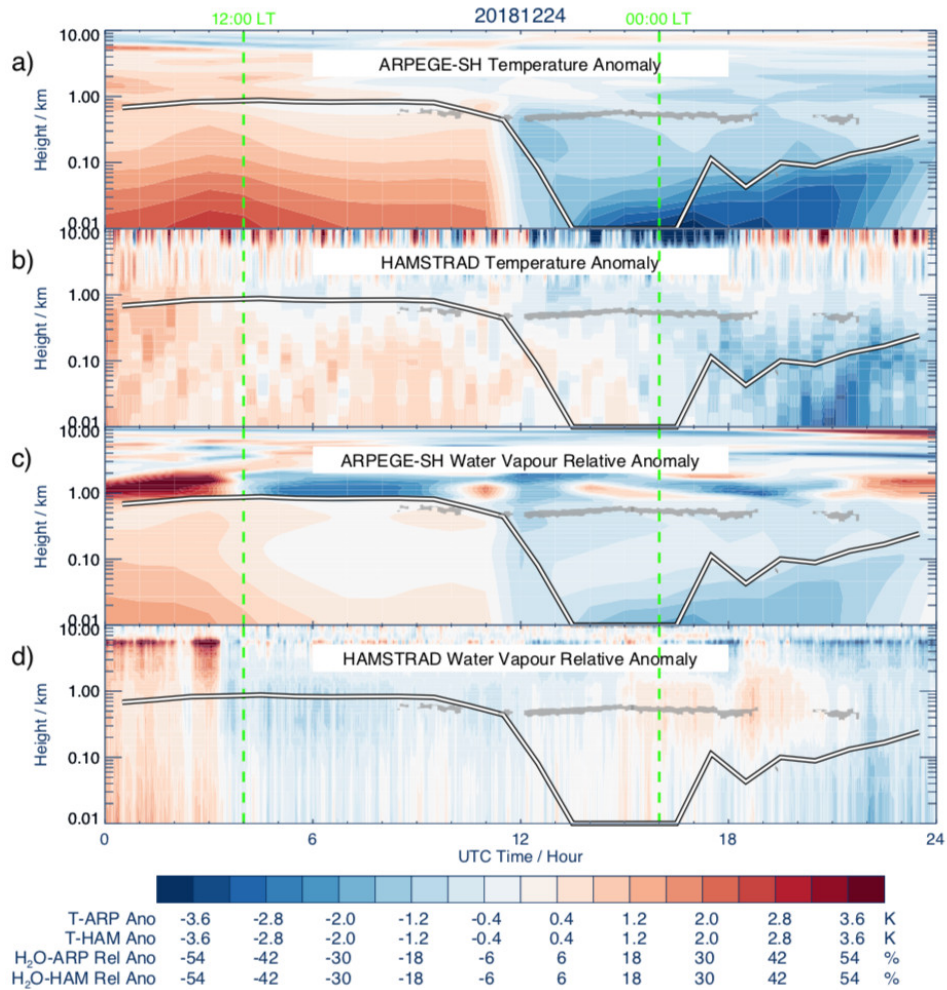
1047



1048

1049 **Figure 5:** CALIOP/CALIPSO spaceborne LIDAR observations version V3.40 along one orbit
 1050 on 24 December 2018 (15:50-16:03 UTC) in the vicinity of Dome C (75°S, 123°E): a) the
 1051 Vertical Feature Mask highlighting a cloud (light blue) near the surface (red circle) and b) the
 1052 Ice/Water Phase Mask highlighting a SLW (dark blue) cloud near the surface (red circle). The
 1053 ground-track of the sensor (pink) has been embedded at the top of the Figure, with the location
 1054 of Dome C marked (red filled circle). Note that the altitude is relative to the sea surface, with
 1055 the height of surface of Dome C at an elevation of 3233 m amsl. Figure adapted from the
 1056 original image available at [https://www-](https://www-calipso.larc.nasa.gov/products/lidar/browse_images/std_v34x_showdate.php?browse_date=2018-12-24)
 1057 [calipso.larc.nasa.gov/products/lidar/browse_images/std_v34x_showdate.php?browse_date=20](https://www-calipso.larc.nasa.gov/products/lidar/browse_images/std_v34x_showdate.php?browse_date=2018-12-24)
 1058 [18-12-24](https://www-calipso.larc.nasa.gov/products/lidar/browse_images/std_v34x_showdate.php?browse_date=2018-12-24).

1059

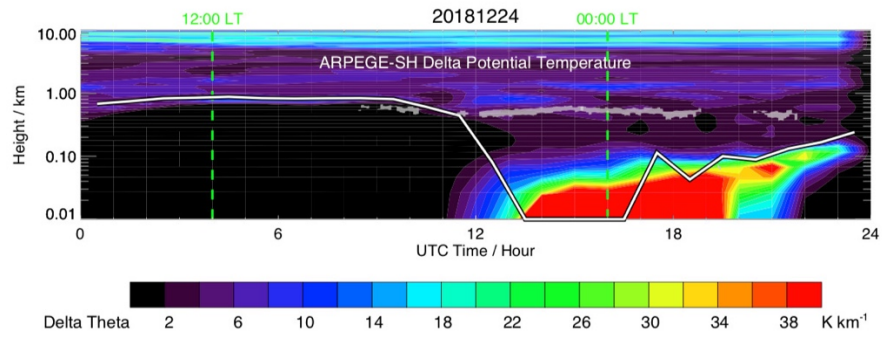


1060

1061 **Figure 6:** Time-height cross section on 24 December 2018 (UTC Time) of a) the temperature
 1062 anomaly (K) calculated by ARPEGE-SH and b) observed by HAMSTRAD, c) the water vapour
 1063 relative anomaly (%) calculated by ARPEGE-SH and d) observed by HAMSTRAD.
 1064 Superimposed to all the Figures are the SLW cloud altitude (grey area) deduced from the
 1065 LIDAR observations (see Fig. 1c) and the top of the Planetary Boundary Layer calculated by
 1066 the ARPEGE-SH model (black-white thick line). Two vertical green dashed lines indicate 12:00
 1067 and 00:00 LT.

1068

1069

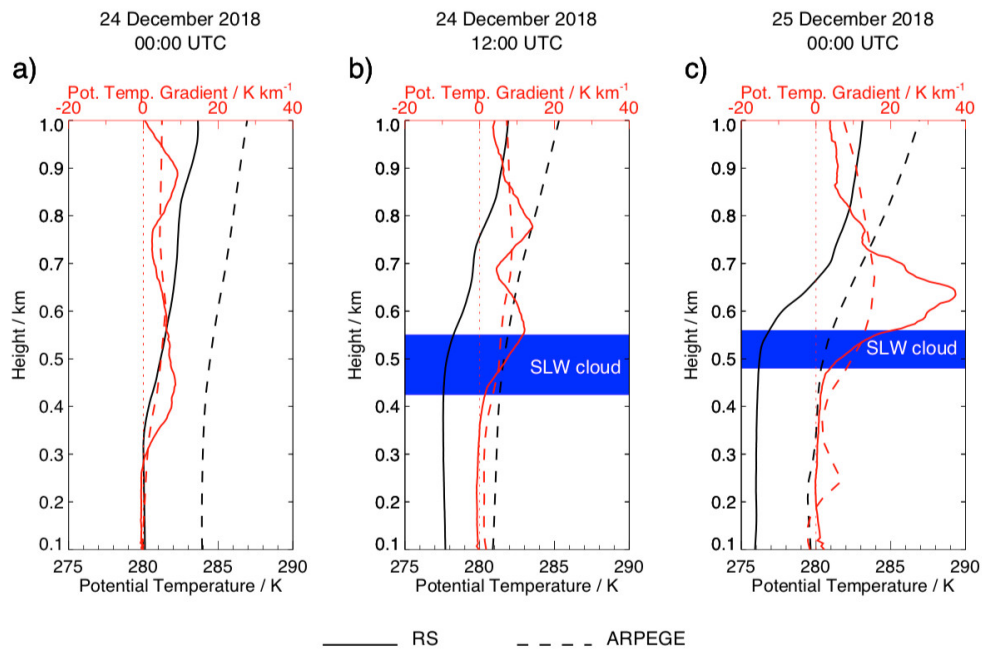


1070

1071 **Figure 7:** Time-height cross section of $\partial\theta/\partial z$ (K km^{-1}) calculated from ARPEGE-SH
 1072 temperature on 24 December 2018 (UTC Time). Superimposed are the SLW cloud altitude
 1073 (grey area) deduced from the LIDAR observations (see Fig. 1) and the top of the Planetary
 1074 Boundary Layer calculated by the ARPEGE-SH model (black-white thick line). Two vertical
 1075 green dashed lines indicate 12:00 and 00:00 LT.

1076

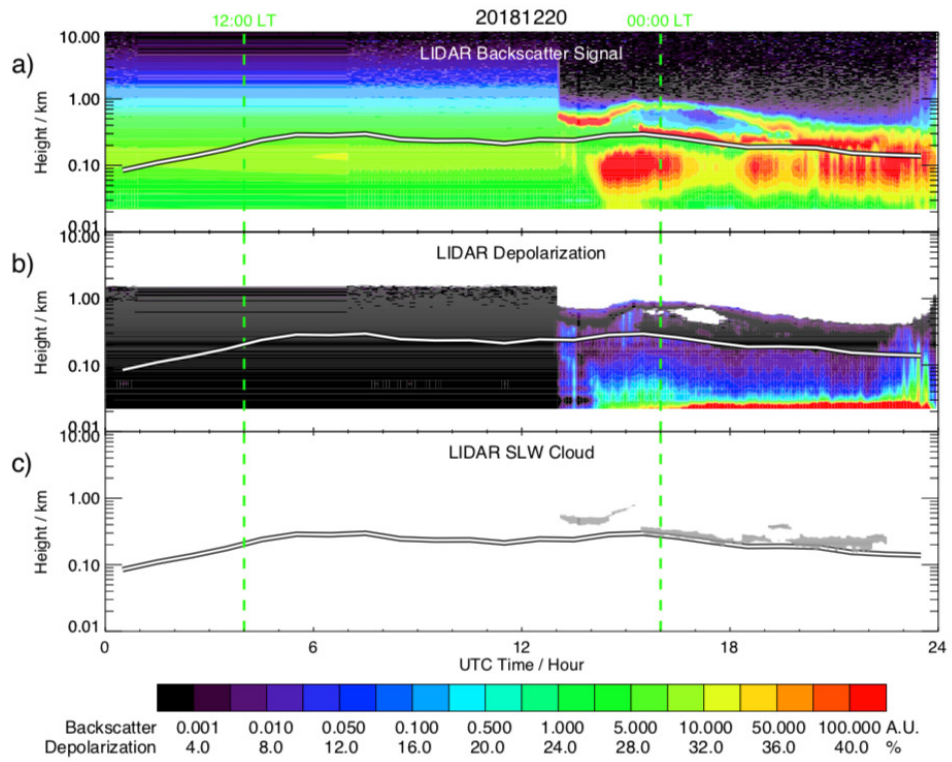
1077



1079

1080 **Figure 8:** Vertical profiles of potential temperature θ (black) and the gradient in potential
 1081 temperature $\partial\theta/\partial z$ (red) as calculated from temperature measured by the radiosondes (solid line)
 1082 and analysed by ARPEGE-SH (dashed line) at Dome C on 24 December 2018 at a) 00:00 and
 1083 b) 12:00 UTC, and c) on 25 December 2018 at 00:00 UTC. The presence and the depth of the
 1084 SLW cloud detected from LIDAR observations are indicated by a blue area.

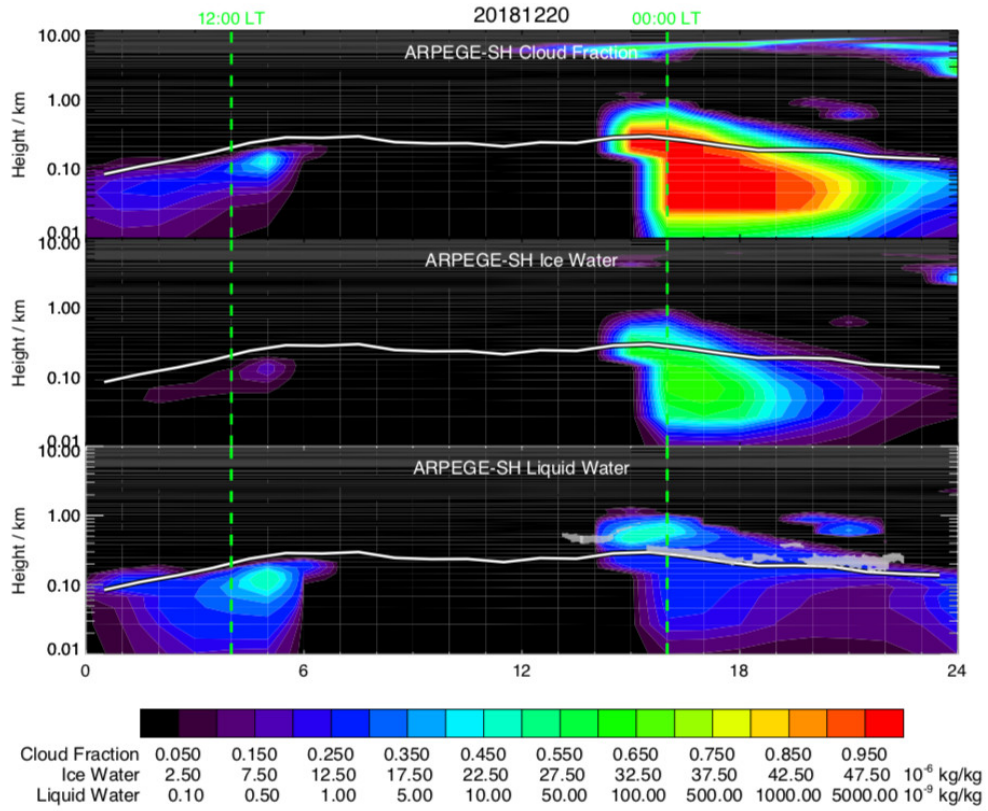
1085



1086

1087 **Figure 9:** Same as Figure 2 but for 20 December 2018.

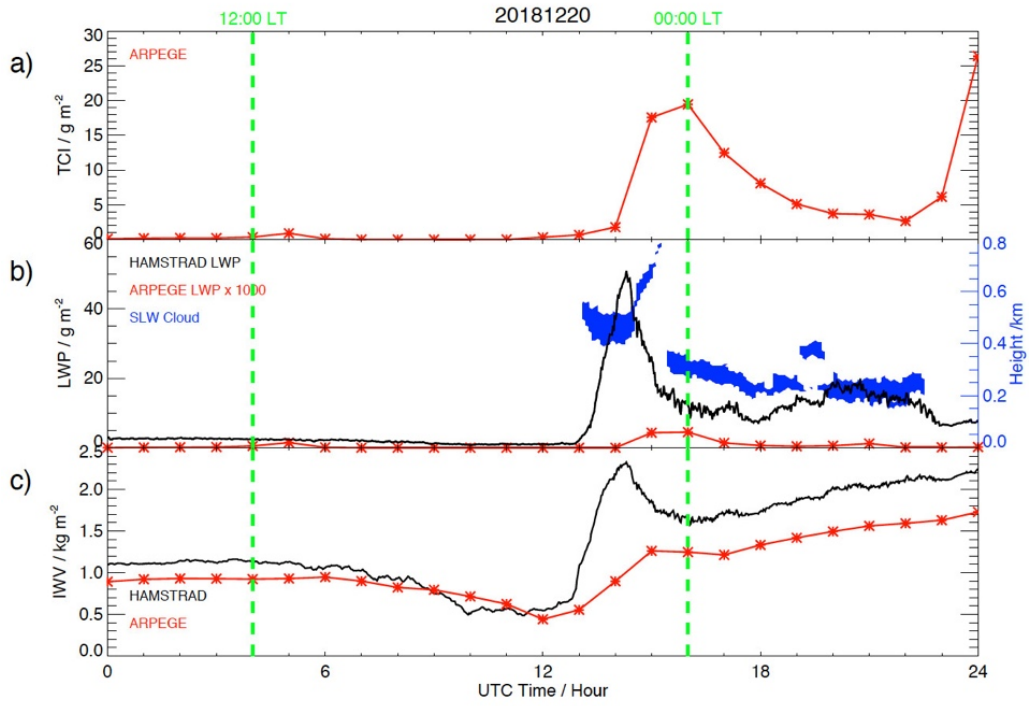
1088



1089

1090 **Figure 10:** Same as Figure 3 but for 20 December 2018.

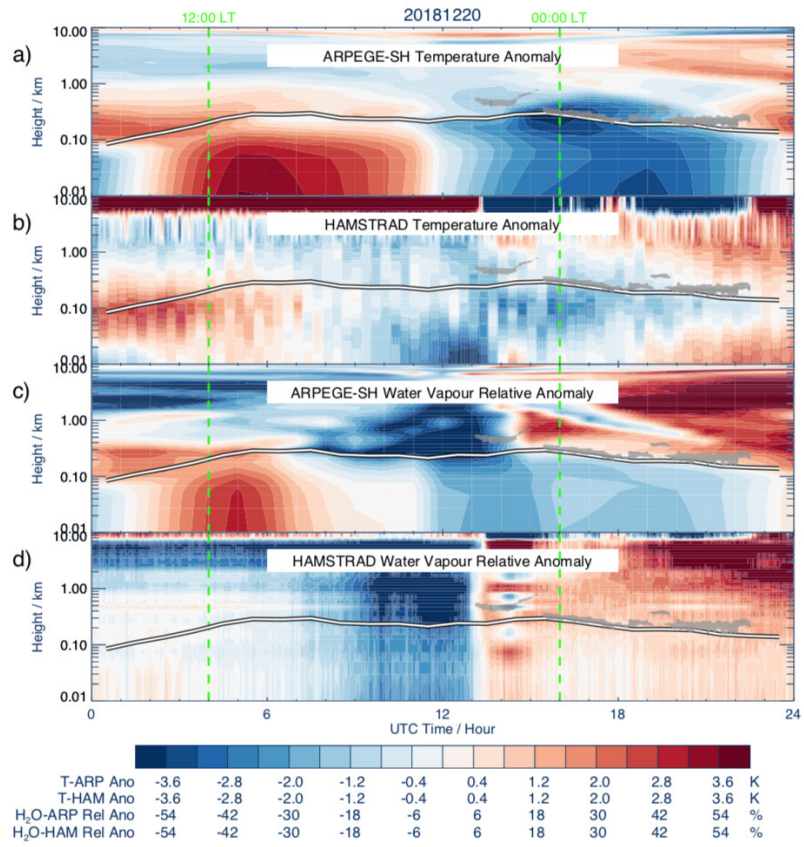
1091



1092

1093 **Figure 11:** Same as Figure 4 but for 20 December 2018.

1094



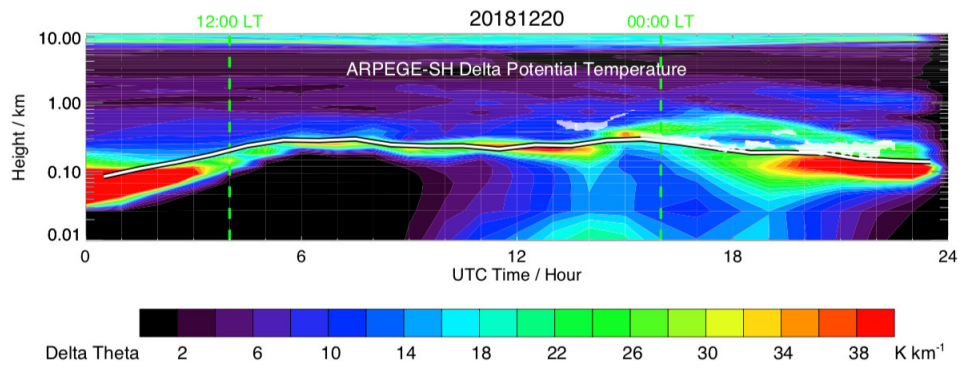
1095

1096 **Figure 12:** Same as Figure 6 but for 20 December 2018.

1097

1098

1099

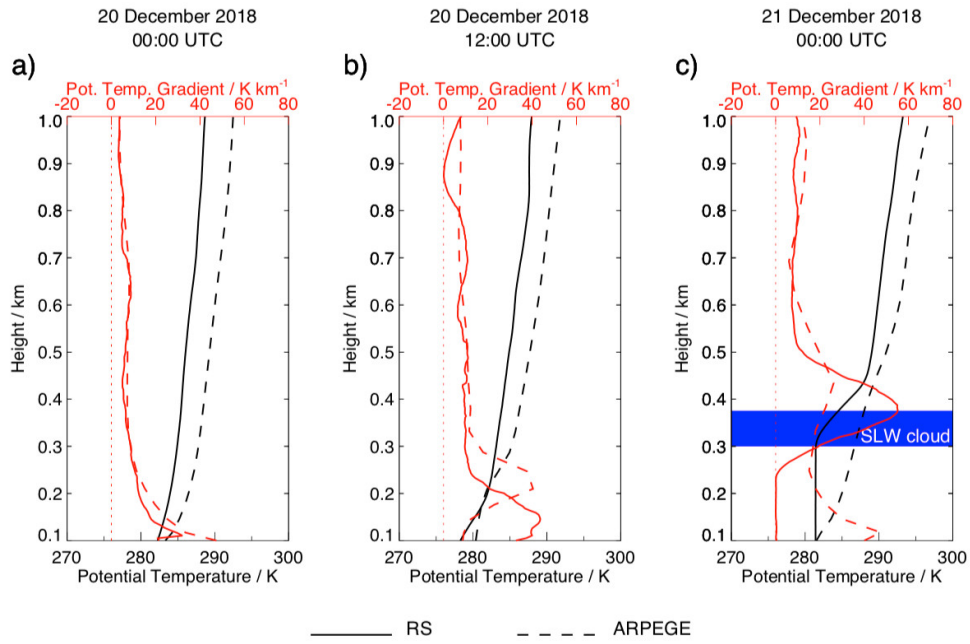


1100

1101 **Figure 13:** Same as Figure 7 but for 20 December 2018.

1102

1103

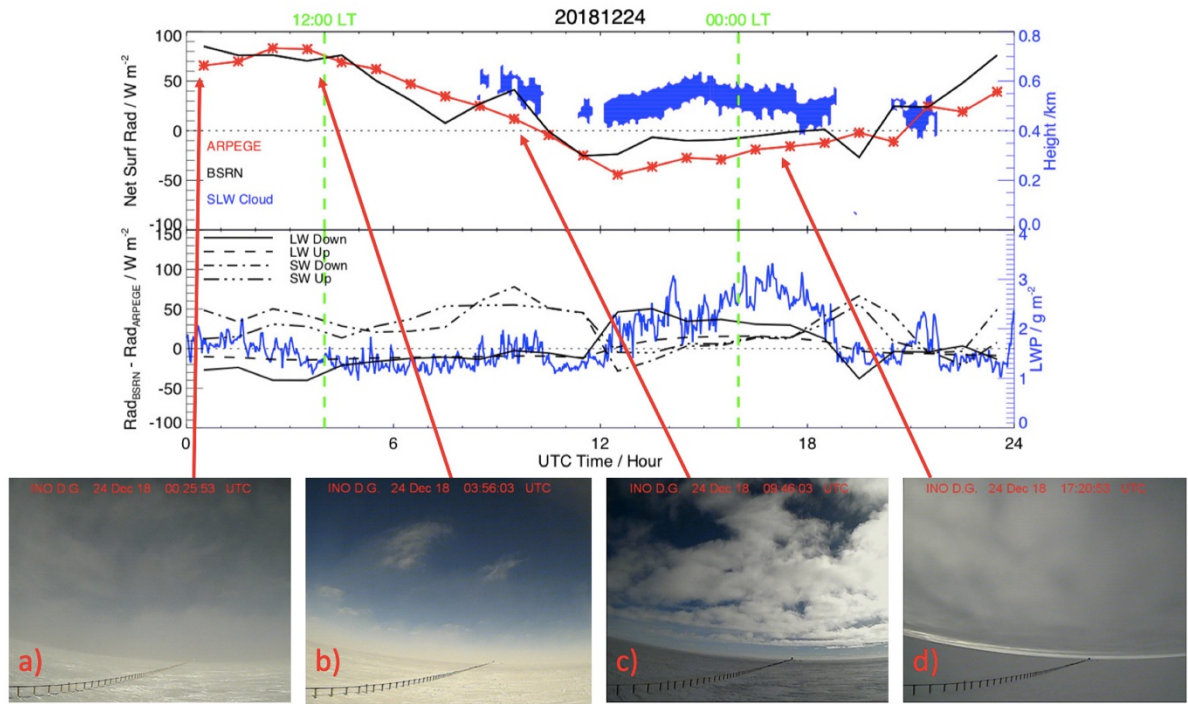


1104

1105 **Figure 14:** Same as Figure 8 but on 20 December 2018 at a) 00:00 and b) 12:00 UTC, and c)

1106 on 21 December 2018 at 00:00 UTC.

1107



1108

1109 **Figure 15:** (Top) Diurnal variation of the net surface radiation ($W m^{-2}$) observed by BSRN

1110 (black solid line) and calculated by ARPEGE-SH (red crossed line) on 24 December 2018 in

1111 UTC Time. Superimposed is the SLW cloud height (blue) deduced from the LIDAR. (Middle)

1112 Diurnal variation of the difference between surface radiation ($W m^{-2}$) observed by BSRN and

1113 calculated by ARPEGE-SH on 24 December 2018 for longwave downward (black solid),

1114 longwave upward (black dashed), shortwave downward (black dashed dotted) and shortwave

1115 upward (black dashed triple dotted) components. Superimposed is LWP (blue) measured by

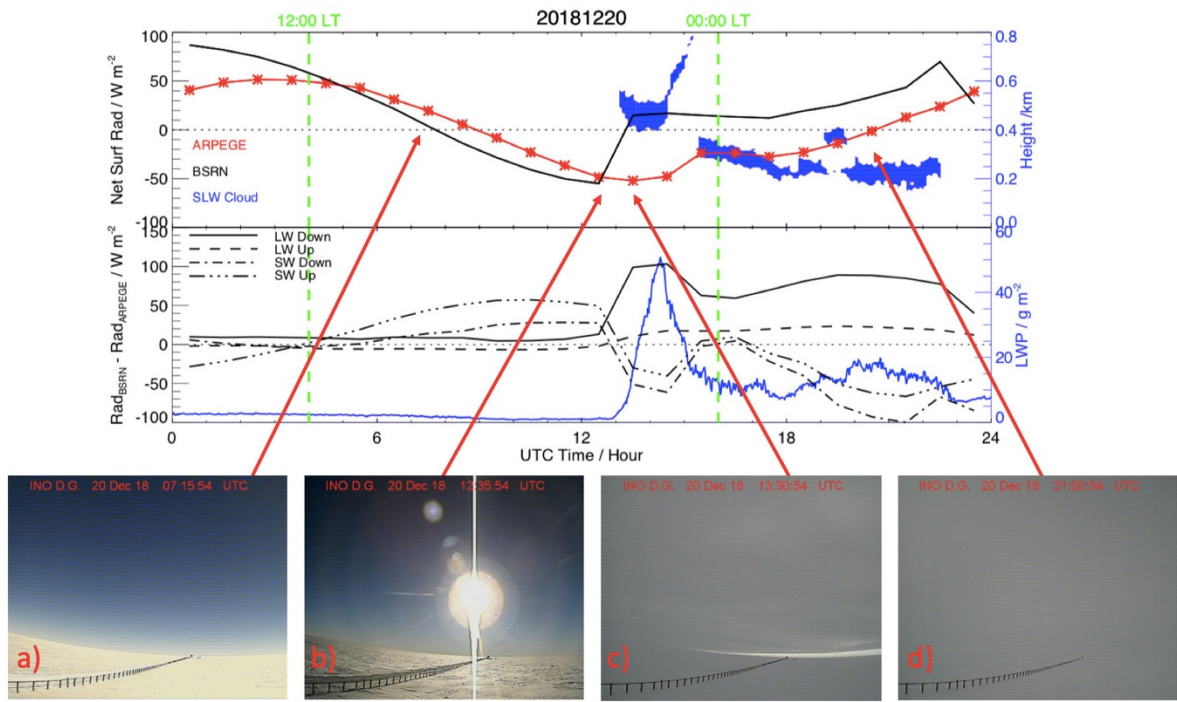
1116 HAMSTRAD. (Bottom) Four webcam images showing the cloud coverage at: a) 00:25 UTC

1117 and b) 03:56 UTC (cirrus clouds, no SLW cloud), c) 09:46 UTC (SLW cloud) and d) 17:20

1118 UTC (SLW cloud). Two vertical green dashed lines indicate 12:00 and 00:00 LT.

1119

1120



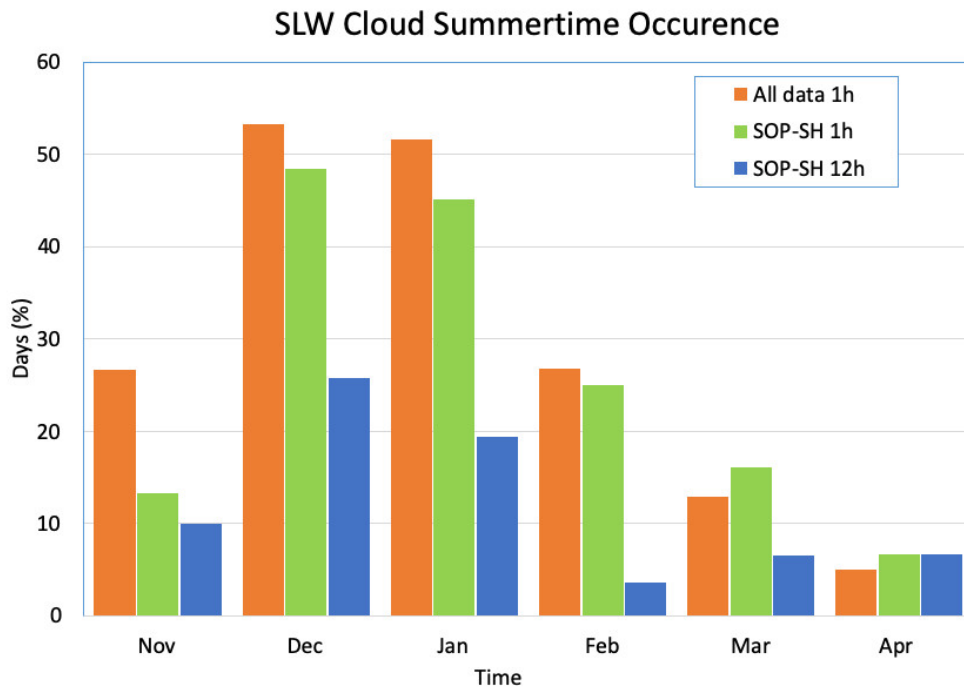
1121

1122 **Figure 16:** Same as Figure 15 but for 20 December 2018 whilst the 4 webcam images were

1123 selected at: a) 07:15 and b) 12:35 UTC (clear sky), c) 13:30 and d) 21:00 UTC (SLW cloud).

1124

1125



1126

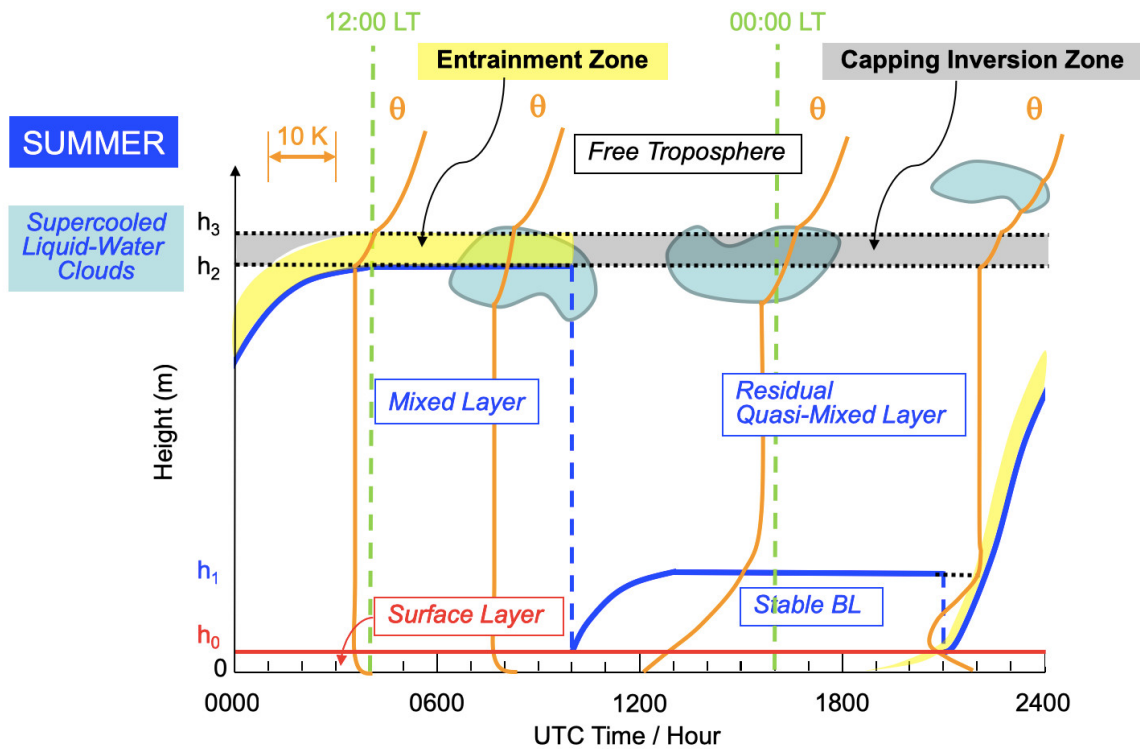
1127 **Figure 17:** Percentage of days per month that SLW clouds were detected within the LIDAR
 1128 data for more than 1 hour per day over different summer periods: “All data 1h” (orange) refers
 1129 to November (2016-2018), December (2016-2018), January (2018-2019), February (2018-
 1130 2019) and March (2018-2019); “SOP-SH 1h” (green) represents the YOPP campaign
 1131 (November 2018 to April 2019). “SOP-SH 12h” (blue) represents the percentage of days per
 1132 month that SLW clouds were detected during the YOPP campaign within the LIDAR data for
 1133 more than 12 hours per day.

1134

1135

1136

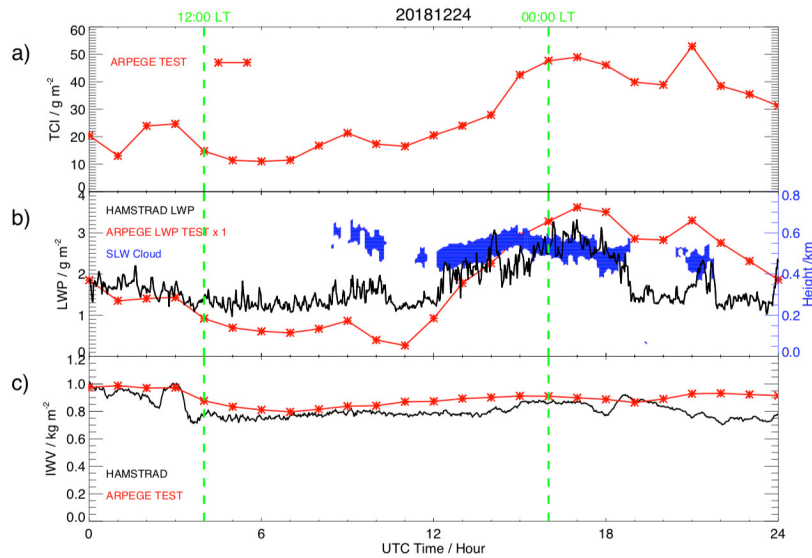
1137



1138

1139 **Figure 18:** Figure modified and updated from Fig. 12 of Ricaud et al. (2012) showing the
 1140 diurnal evolution (UTC Time) of the different layers in the Planetary Boundary Layer (PBL)
 1141 with h_0 the top of the surface layer, h_3 the daily overall top of the PBL, and h_1 the top of the
 1142 intermediate stable layer within the PBL. The orange lines symbolize the vertical profiles of
 1143 potential temperature θ , and the light blue areas the SLW clouds. The layer between h_2 and h_3
 1144 is named “capping inversion zone”. The yellow area represents the “entrainment zone” at the
 1145 top of the (cloudy or cloud-free) mixed layer. When the mixed layer is fully developed, the
 1146 entrainment zone coincides with the capping inversion zone. Note that $LT = UTC + 8$ h,
 1147 midnight and noon in the local time reference being indicated by the green dashed lines.

1148

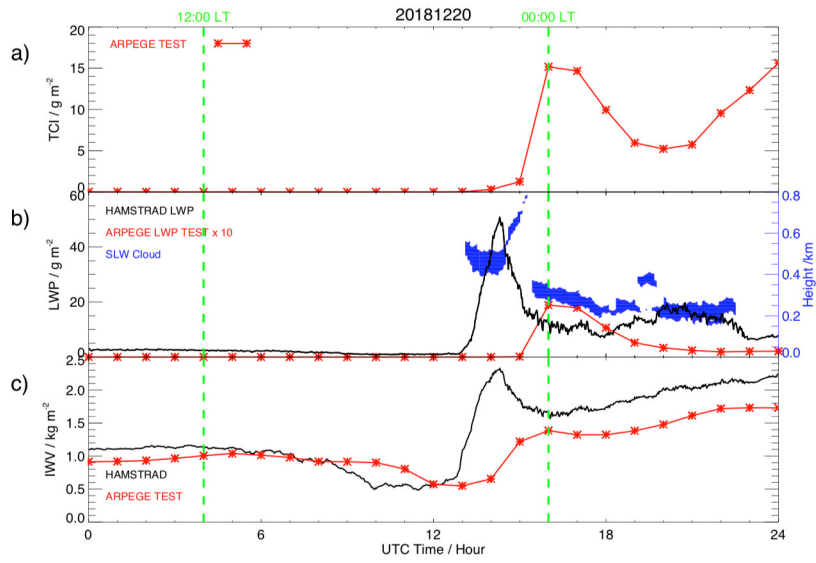


1149

1150 **Figure 19:** Diurnal variation on 24 December 2018 (UTC Time) of: a) the Total Column of Ice
 1151 (TCI) (g m^{-2}) calculated by ARPEGE-SH in test mode (red crossed line), b) the Liquid Water
 1152 Path (LWP) measured by HAMSTRAD (g m^{-2} , black solid line) and calculated by ARPEGE-
 1153 SH in test mode (-no scaling- g m^{-2} , red crossed line) and c) the Integrated Water Vapour (IWV,
 1154 kg m^{-2}) measured by HAMSTRAD (black solid line) and calculated by ARPEGE-SH in test
 1155 mode (red crossed line). Superimposed to panel b) is the SLW cloud thickness (blue area)
 1156 deduced from the LIDAR observations (see Fig. 2c) (blue y-axis on the right of the Figure).
 1157 Two vertical green dashed lines indicate 12:00 and 00:00 LT.

1158

1159



1160

1161 **Figure 20:** Same as Figure 19 but on 20 December 2018 (UTC Time) and LWP from ARPEGE-
1162 SH in test mode has been multiplied by a factor 10.

1163

1164